CHAPTER 3

Poisoning-free CO oxidation over Ni_nCu Cluster

3.1 Introduction

The carbon monoxide (CO) oxidation ($2CO + O_2 \rightarrow 2CO_2$) which is crucial in catalytic conversion of automobile exhausts and low-temperature fuel cells for harmless and environment-friendly emission, is a focus area of interest in the field of fundamental research of various catalytic reactions [1]. Traditionally, platinum group metals (PGMs) (iridium (Ir), rhodium (Rh), platinum (Pt), and palladium (Pd)) are in vogue and single out as superior catalysts for CO oxidation and O_2 reduction [1−3]. No matter which size, shape, or dimensionality it possesses, Pt stands out as the irreplaceable and exceptional electrode material for the fuel cells, oxygen reduction reaction, hydrogen evolution reaction, water-gas shift, hydrogenation, and especially for CO oxidation owing to its remarkable catalytic efficiency as compared to other transition metals (TMs) [4]. To gain molecular-level insights on reactions that occur at Pt surfaces, the nanocluster (NC) form of Pt turns out to be a fundamental topic of investigation for CO oxidation [4-5]. Despite all advantages, the major obstacles in the commercialization of Pt-based catalysts are their overprice, scarcity, and especially the higher affinity towards CO which causes rapid deactivation of the catalyst by CO poisoning [6-7]. Thus, the main purpose of designing heterogeneous catalysts by trimming or preventing the usage of traditional PGMs while retaining their catalytic activity has been elevated for years [8]. Principally, two major strategies are available to circumvent CO poisoning: (1) desorption of CO operating at the elevated temperature and (2) alloying of less reactive metals such as Cu, Ag, and Au with parent material [8-9]. The first strategy appears to be unfeasible and expensive in terms of high reaction temperature which resulted in low coverages for important reactants and the risk of deactivation [9]. In contrast, the second tactic appears convincing due to the higher tolerance to CO poisoning while retaining reasonable activity and cost-effectiveness [10−12]. For that matter, testimonials with optimized performance and design of low-cost catalysts after alloying, count on a

fundamental understanding of the electronic structure (in particular the d-states) of an ensemble of surface atoms and its relationship with the energetics of adsorbate−surface interactions [13-14]. The *d-band* center (ε_d) is a vital electronic reactivity descriptor derived from the *d-band* model which is proven to be extremely useful in search of optimal catalytic materials [15]. The number of studies on alloying of Pt-M (M = Ru, Sn, Ge, Mo, and Cu) revealed that the alloying modified the electronic structure of Pt via charge transfer from dopant to Pt and is responsible for the weaker adsorption of CO (lower affinity toward CO) [12,16-17]. To avoid poisoning of Pt during CO oxidation reaction, the role of Co, Ni, and Cu doping over free-standing and supported Pt clusters is systematically reported by Ahmad et al. [10] along with a novel design strategy of *d-band* center inversion. Taking over the place of precious Pt catalyst by a nonprecious metal, nickel (Ni), gathered our whole attention through its low cost and catalytic activity which is as good as that of Pt [18-19]. Despite a significant number of experimental and theoretical reports on Ni and Ni-based nanostructures [20−22], the complete elimination of CO poisoning over Ni is still unresolved and is a topic of debate. To overcome this barrier, the alloying of Ni clusters with second low-cost coinage metal such as copper (Cu) is the main concern of this study. In contradiction to the Ni, only a few studies have been reported on the Ni−Cu alloys [23-24]. The rational design of efficient and highly active catalysts requires an understanding of the origin of catalytic activity on account of energetics and interactions that occur at the atomic level which cannot be easily measured by experiments performed in real conditions such as composition at an atomic level, the structural fluxionality, modulation in the electronic structure of surface atoms, charge transfer mechanism, and interaction among adsorbent−adsorbate throughout the reaction pathway [2].

Thus, this work comprises the results of a study on the structural and electronic properties of Ni$_{n+1}$ and Ni$_n$Cu clusters (1 ≤ n ≤ 12) by employing spin-polarized DFT calculations. Our main interest is to elucidate the influence of substitutional doping of a

single Cu atom on the adsorption of CO and also to investigate the effect of CO poisoning over clusters. The present work reveals the kinetics of CO oxidation reaction over Ni_9, Ni_{13}, Ni_8Cu, and Ni_{12}Cu clusters.

3.2 Computational methods and theoretical analysis

All self-consistent total energy calculations were based on spin-polarized density functional theory as implemented in the Quantum ESPRESSO (QE) package [25-26]. Electron−ion interactions were described using all-electron projector-augmented wave (PAW) pseudopotentials [27]. Electronic exchange-correlation interactions were evaluated by the local density approximation (LDA) proposed by Perdew-Zunger [28] and generalized gradient approximation (GGA) formulated by Perdew-Burke-Ernzerhof (PBE) [29]. The periodic images were separated by 18 Å vacuum in all three directions. Brillouin zone (BZ) was sampled at the Γ-point. The plane-wave basis set with a kinetic cut-off energy of 55 Ry was chosen for geometry relaxation. To improve the convergence of states near the Fermi level, the Methfessel-Paxton smearing method with a finite temperature width of 0.02 Ry was adopted [30]. The convergence threshold for geometry optimization was set to 1.0×10^{-6} eV without applying any symmetry constraint. The position of all atoms residing in clusters was fully optimized until the Hellmann–Feynman force on each atom is less than 1.0×10^{-4} eV/Å (using the Broyden−Fletcher−Goldfarb−Shanno (BFGS) algorithm) [31]. To elucidate the compactness of clusters and recognize their putative global minimum structures, the effective coordination number (ECN) and averaged bond length (d_{av}) approach was taken into consideration. The average ECN and d_{av} for each configuration are obtained by,

$$ECN = \frac{1}{N}\sum_{i=1}^{N} ECN_i \qquad (3.1)$$

$$d_{av} = \frac{1}{N}\sum_{i=1}^{N} d_{av}^i \qquad (3.2)$$

where N is the total number of atoms in the cluster [32-33]. For the treatment of the long-range dispersion forces, the semi-empirical van der Waals corrections D2 and D3 proposed by S. Grimme were employed [34-35] for the accurate prediction of adsorption properties (more information is provided in chapter 2). The vibrational frequencies of adsorbed CO are computed with the density-functional perturbation theory (DFPT) approach [36]. The *d-band* model introduced by Bhattacharjee and co-workers (modification of Nørskov and Hammer *d-band* model) [37-38] for the spin-polarized DFT calculations have been adopted to determine the electronic descriptors i.e., *d-band* center, *d-band* width (W_d) and fractional filling of *d-band* (f_l) (for both spin-up and spin-down states) using Eqn. (2.27) - (2.29). The minimum energy path (MEP) and transition state for CO oxidation were sketched out using the climbing image nudged elastic band (CI-NEB) method proposed by Henkelman et al. (implemented in the Quantum ESPRESSO) [39-40]. In each elementary step, five intermediate images were interpolated between initial and final states. Similar convergence criteria and computational parameters (including the PBE+D3 approach) were adopted for the investigation of reaction path, as considered for geometry relaxation. The activation energy barrier (E_a) for each reaction step was obtained using the following formula,

$$E_a = E_{TS} - E_{IS/IM} \tag{3.3}$$

where, E_{TS} and $E_{IS/IM}$ respectively are the energies of initial and transition states/intermediate states that depend on the nature of the reaction. In this study, all the pictorial representations of structures, HOMO-LUMO, and charge density differences were prepared by the XCrySDen and Vesta visualization packages [41-42].
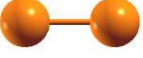
3.3 Results and Discussion

3.3.1 Ni$_{n+1}$ and Ni$_n$Cu clusters (1 ≤ n ≤ 12)

Structures. To ensure the validity of the adopted computational method, the binding energy per atom and bond length of Ni$_2$, NiCu, and Cu$_2$ systems were calculated

using LDA and PBE functionals and presented in Table 3.1. The computed values

obtained with PBE functional are in good agreement with experimental [43-44] and other

theoretical data [45−47] as compared to LDA functional.

Table 3.1: Comparison of computed data for the Ni$_2$, NiCu, and Cu$_2$ clusters with
experimental and other theoretical data.

System	Studies	Type	Bond length (Å)	E$_b$ (eV/atom)
Ni$_2$ [$D_{\infty h}$ (Dimer)]	Morse et al. [43]	Experimental	2.155	1.034
	Castro et al. [45]	Theoretical	2.10	1.74
	Granja-DelRío et al. [46]	Theoretical	2.08	1.47
	Ours (LDA)		2.04	1.76
	Ours (PBE)		2.10	1.32
NiCu [$C_{\infty v}$ Linear)]	Spain et al. [44]	Experimental	2.23	1.025
	Boulbazine et al. [47]	Theoretical	2.22	1.20
	Ours (LDA)		2.14	1.46
	Ours (PBE)		2.20	1.15
Cu$_2$ [$D_{\infty h}$ (Dimer)]	Morse et al. [43]	Experimental	2.22	1.01
	Boulbazine et al. [47]	Theoretical	2.21	1.26
	Ours (LDA)		2.15	1.45
	Ours (PBE)		2.23	1.22

To determine the lowest-energy structures of Ni$_{n+1}$ clusters ($2 \leq n \leq 12$), possible

geometries were inspected and summarized in Figure A.1 of Appendix A.1 with their

corresponding relative energy (ΔE). For Ni$_n$Cu clusters, one Cu atom is introduced into

Ni$_{n+1}$ clusters at different positions. The complete geometrical search with LDA and PBE

functionals for Ni$_n$Cu clusters is presented in Figure A.2 of Appendix A.2. The most

stable clusters ($\Delta E = 0$) with PBE functional are considered as the representative

systems throughout the study and are shown in Figure 3.1. For better visualization, the

skeleton construction of these Ni$_{n+1}$ and Ni$_n$Cu ($2 \leq n \leq 12$) clusters along with their

corresponding effective coordination number (ECN; computed using Eqn. (3.1)) and

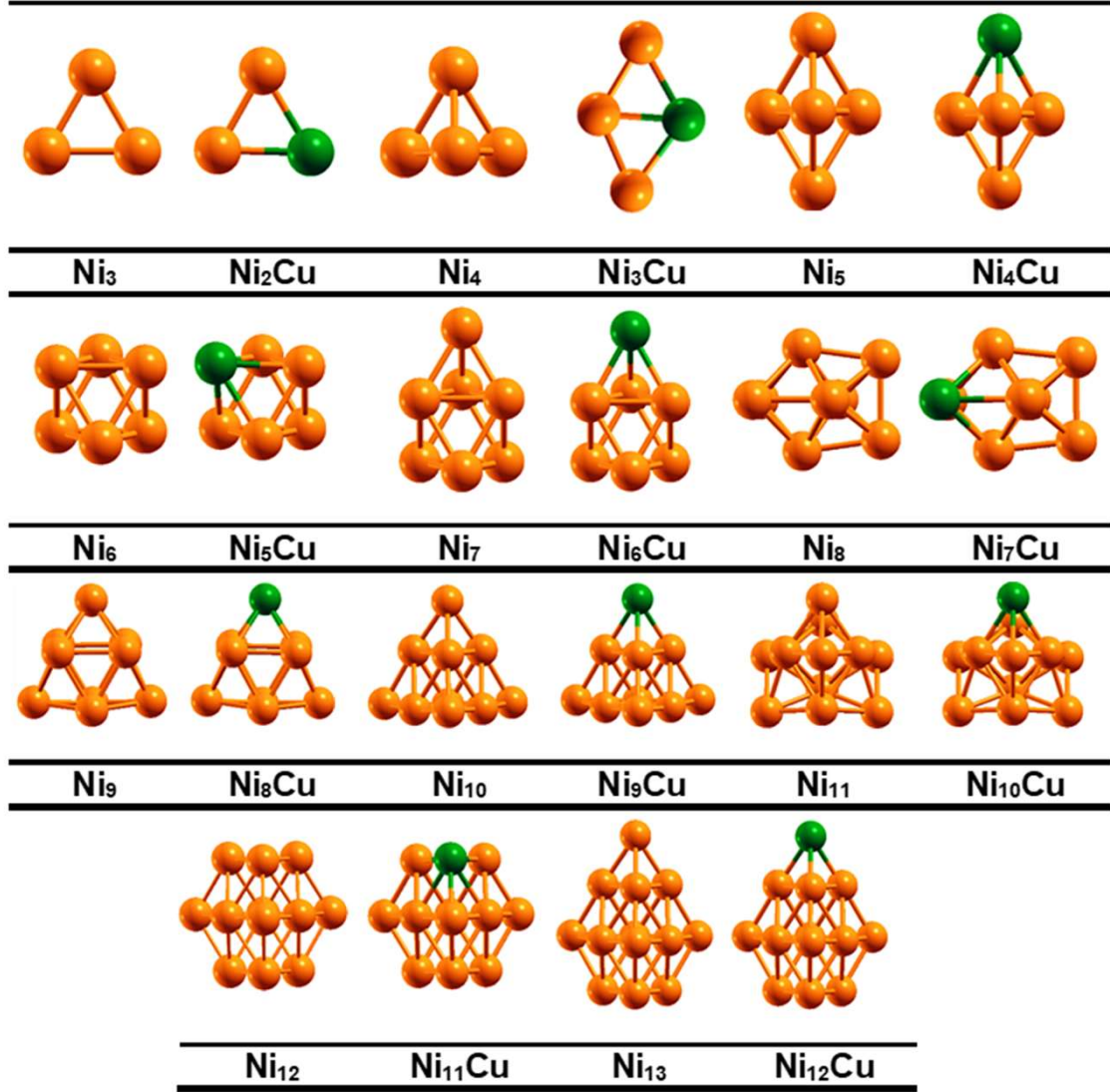point-group symmetry (structure) are presented in Figures 3.2-3.3, respectively.

Figure 3.1: Lowest-energy structures (obtained with PBE functional) of the Ni$_{n+1}$ and Ni$_n$Cu cluster ($2 \leq n \leq 12$).

The point-group symmetry (structure) examined with LDA functional for pure and Cu doped Ni clusters is provided in Appendix A.3. The mixing energy per atom (E_{mix}) (obtained with LDA functional) and fragmentation energy of Ni$_n$Cu clusters ($1 \leq n \leq 12$) (obtained with LDA and GGA functional) are presented in Table A.1 of Appendix A.3. Our results on ECN and point-group symmetry (structure) of pure Ni clusters fall within the other reports [46,48]. Interestingly, for Ni$_{13}$, icosahedral geometry is recognized as the lowest energy structure by LDA functional, while, the PBE functional shows preference for the hcp one [48].
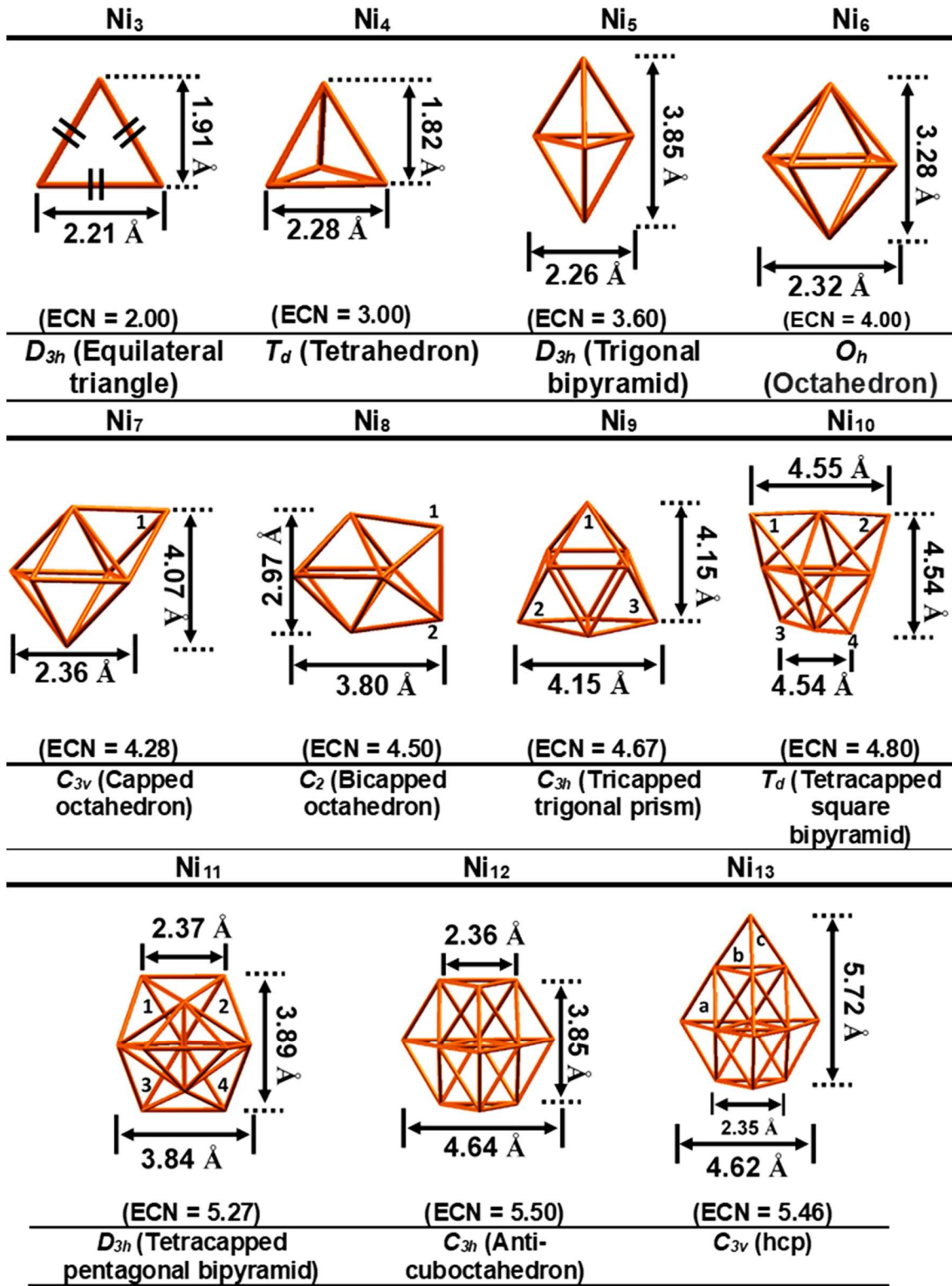
Figure 3.2: Skeleton representation of lowest-energy structures of the Ni$_{n+1}$ cluster ($2 \leq n \leq 12$) with their corresponding effective coordination number (ECN) and point-group symmetry (structure).
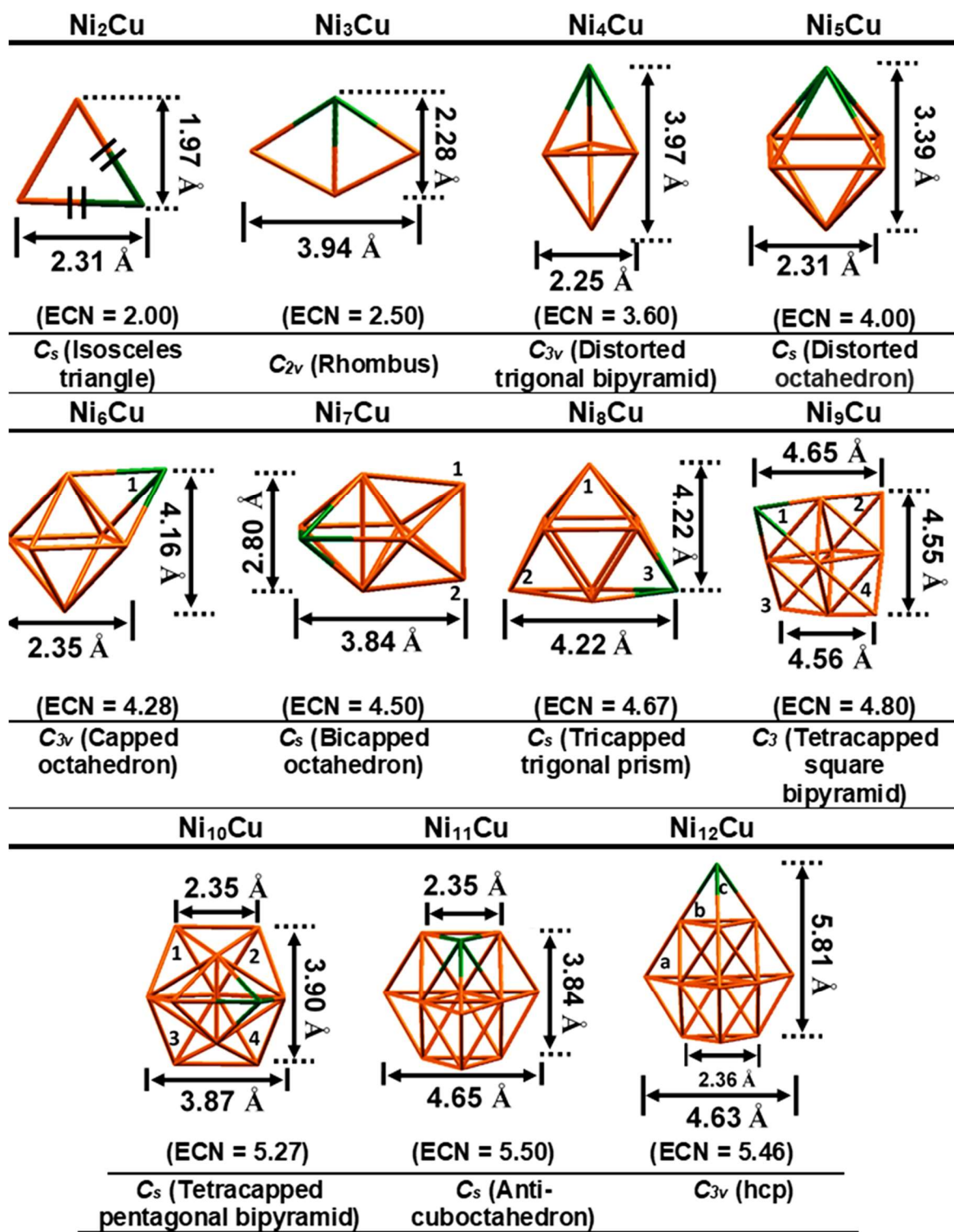
Figure 3.3: Skeleton representation of lowest-energy structures of the Ni_nCu cluster ($2 \leq n \leq 12$) with their corresponding effective coordination number (ECN) and point-group symmetry (structure).

As shown in Figures 3.1 and 3.3, the lowest-energy structure of Ni$_n$Cu clusters (2 ≤ n ≤ 12) yields geometries that are similar to those of pure Ni clusters with a slight deformation, except for n = 3, which adopts the rhombus structure. For the size range of n = 4 to 12, Ni$_n$Cu clusters exhibit 3D configurations [47,49]. The pictorial representation of most stable Ni$_n$Cu clusters in Figure 3.1 shows that the Cu atom prefers the vertex position for n = 4, 5, 8, 9, and 12, capped position for n = 6, 7, and 10, and at the upper plane of a cluster for n = 11. After energy optimization, the structural stability is assessed by examining the average bond length of clusters using equation 3.2. The plot of computed average bond length (with LDA and PBE functional) for energetically favorable pure as well as Cu doped Ni clusters are provided in Figure A.3(a-b) of Appendix A.4 which indicates that the average bond length of clusters increases after Cu doping. This piece of information shows the direct relationship between the occupancy of the Cu atom at a low-connectivity vertex (or capped position) that reduces the number of Ni–Cu bonds and results in the elongation of bond distance, where those are weaker than Ni–Ni bonds.

3.3.2 Ni K-edge XANES

The X-ray absorption near-edge spectroscopy (XANES) is a powerful technique to reveal and extract information such as oxidation state and geometry of the systems. XANES spectra are mainly divided into two parts namely pre-edge (lower energy region) and rising edge (higher energy region) regions. The low-intensity peak observed at a pre-edge region of XANES spectra is called the pre-edge peak which provides valuable insight on the ligand field, spin states, and centrosymmetry of the site. The rising edge region covers two important features i.e., rising edge peak and white line peak. Herein, XANES spectra were calculated using the finite difference method (FDM) and Hedin-Lundqvist exchange-correlation potential implemented in the FDM near-edge structure (FDMNES) ab initio package [50-51].
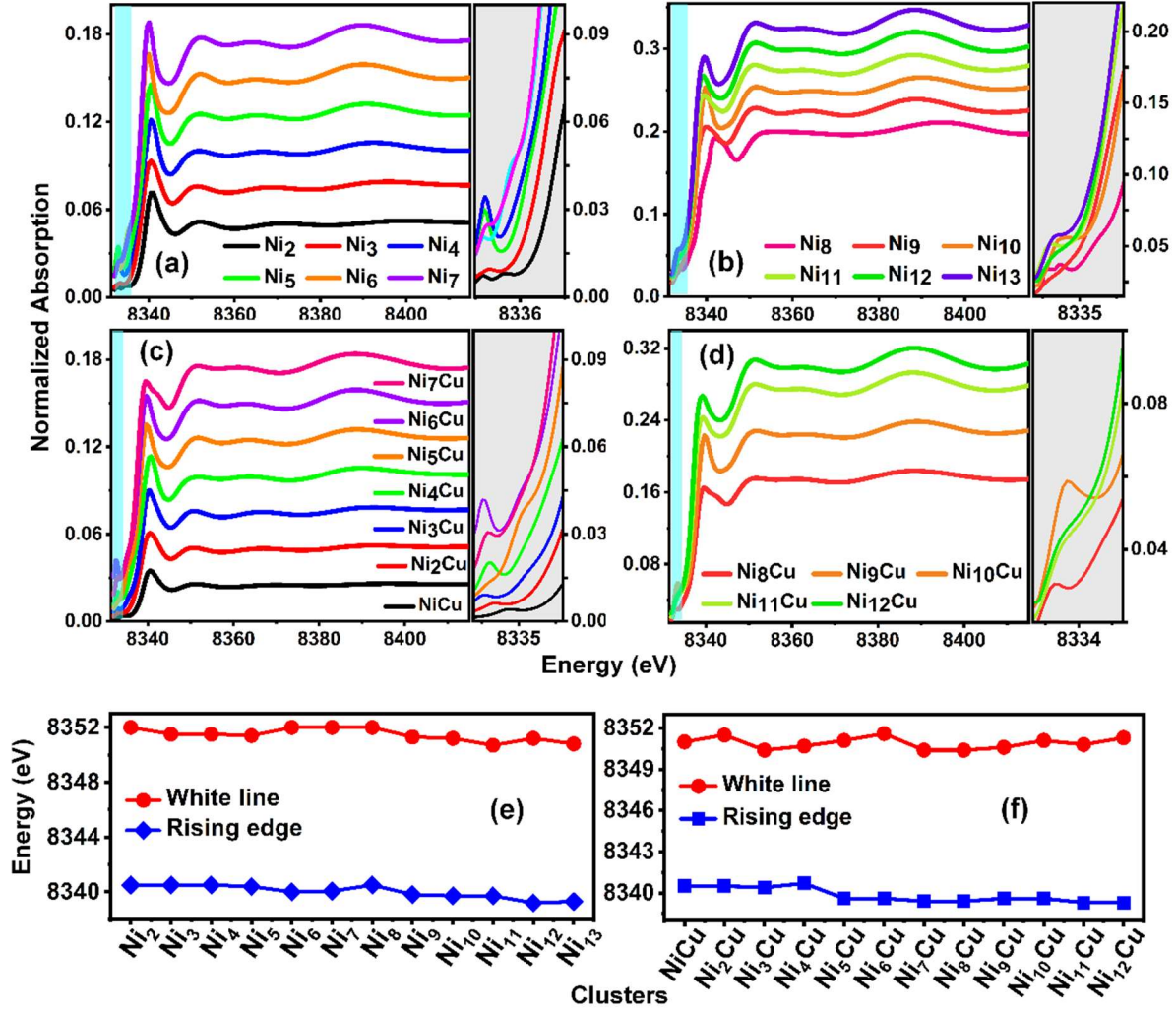
Figure 3.4: Simulated XANES spectra of (a-b) Ni$_{n+1}$ clusters and (c-d) Ni$_n$Cu clusters (1 ≤ n ≤ 12). The shaded area in cyan color represents the pre-edge region and its enlarged counterparts shown in the right panel of the corresponding XANES spectra. The calculated E$_{rising-edge}$ (blue color) and E$_{white-line}$ (red color) peaks corresponding to the (e) Ni$_{n+1}$ clusters and (f) Ni$_n$Cu clusters (1 ≤ n ≤ 12).

The radius of the calculated cluster to compute Ni K-edge spectra of Ni$_{n+1}$ and Ni$_n$Cu clusters is fixed to 3 Å. The calculated Ni K-edge XANES spectra of Ni$_{n+1}$ and Ni$_n$Cu clusters are presented in Figure 3.4(a-d). It is seen from Figure 3.4(a-d) that the low-intensity pre-edge peak positioned at around 8332−8335 eV for both kinds of cluster systems is consistent with the previous theoretical and experimental data [52]. This low-intensity pre-edge peak in the Ni K-edge spectra provides information on the local electronic structure at the absorbing Ni atoms in the presence of the core-hole. Under

this phenomenon, the Ni K-edge absorption is caused by the transition of a 1s electron of Ni from its core atomic state to a final unoccupied state (1s → 3d transition). Experimentally, the identification of this peak is tough as it is a dipole ($\Delta l = \pm 1$) forbidden but quadruple ($\Delta l = 0, \pm 2$) allowed transition. Successively, the energy variation corresponding to the rising edge and white line peak for the Ni_{n+1} and Ni_nCu clusters is plotted in Figure 3.4(e-f), respectively. Herein, the increment(decrement) in the energy corresponding to both the rising-edge and the white line peaks confirm the increment (decrement) in the oxidation state of Ni. As expected, Cu doping lowers the energy of rising edge and white line peak of systems which resulted in the decrement in the oxidation state of the Ni and is accountable for lowering the affinity of systems toward CO molecule [53]. It is noticed from Figure 3.4(a-d) that a hump-like shape appears in the energy range 8380 eV−8400 eV as the size of the cluster increases. These pronounced features scanned from Ni K-edge spectra of Ni_{n+1} and Ni_nCu clusters will assist the experimentalists in the identification of geometric and electronic structures at the nanoscale.

3.3.3 Structural stability and energetics

To inspect whether the nanoalloy formation is either energetically favorable or not, the mixing (or excess) energy per atom [54-55] was examined to quantify the relative energetic stability of Ni_nCu clusters by using the following formula,

$$E_{mix}(Ni_nCu) = \frac{1}{n+1}\left[E(Ni_nCu) - \frac{n}{n+1}E(Ni_{n+1}) - \frac{1}{n+1}E(Cu_{n+1})\right] \qquad (3.4)$$

where, $E(Ni_nCu)$, $E(Ni_{n+1})$ and $E(Cu_{n+1})$ represent the total energy of the lowest-energy structures of Ni_nCu, Ni_{n+1}, and Cu_{n+1} clusters respectively. n represents the number of atoms. Note that geometries of Cu_{n+1} clusters identical to Ni_{n+1} clusters were optimized too with LDA and PBE functional. The mixing energy per atom for Ni_nCu clusters (with PBE functional) is presented in Figure 3.5.
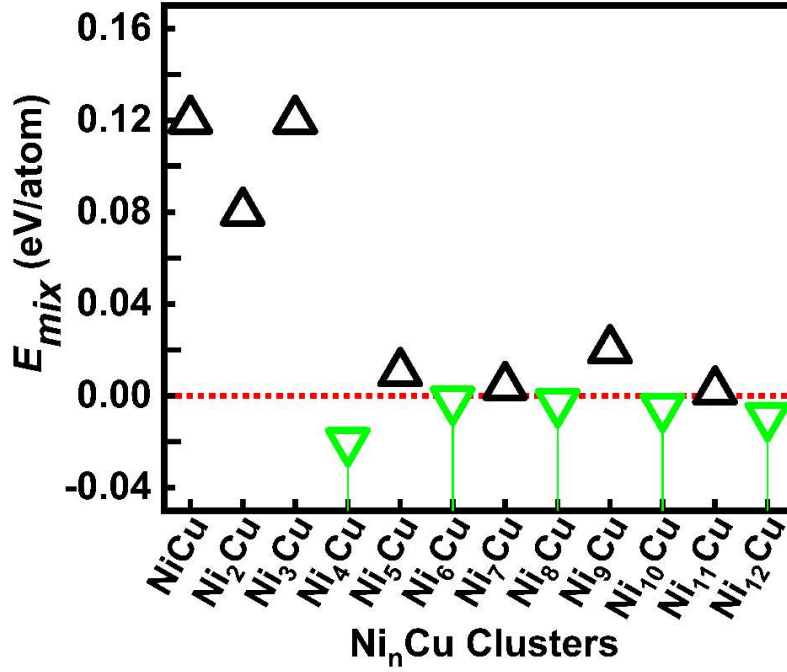
Figure 3.5: Mixing energy per atom (E_{mix}) of Ni$_n$Cu clusters ($1 \leq n \leq 12$). The black and light green symbols represent the positive and negative value of (E_{mix}), respectively.

A negative value of mixing energy represents favorable mixing (thermodynamical stability of the formation/composition of alloys), whereas demixing (a tendency of segregation among the two species of constituent atoms) is indicated by a positive value. From Figure 3.5, we observed that the formation of Ni$_4$Cu, Ni$_6$Cu, Ni$_8$Cu, Ni$_{10}$Cu, and Ni$_{12}$Cu clusters is energetically favorable and the mixing of Ni$_4$Cu cluster is highly favorable with a maximum negative value. The rest of the Ni$_n$Cu clusters exhibit a demixing tendency with positive energy values. The detailed theoretical analysis of the relative energetic stabilities (i.e., average binding energy per atom, second-order energy difference, and fragmentation energy) and magnetic properties of Ni$_{n+1}$ and Ni$_n$Cu clusters (obtained with LDA and PBE functionals) are presented in Figure A.3(c-g) of Appendix A.4. The calculated value of E_{mix}(Ni$_n$Cu) (with LDA functional) and $\Delta E_F(Cu)$ (with LDA and PBE functionals) of Ni$_n$Cu clusters are provided in Table A.2 of Appendix A.4. Also, the systematic analysis and determination of spin-dependent quantum chemical descriptors (attained with PBE functional) such as highest occupied molecular orbital (HOMO)-lowest unoccupied molecular orbital (LUMO) energy gap

(E_g), electronegativity (χ), global hardness (η), global softness (S), and an electrophilicity index (ω) for Ni_{n+1} and Ni_nCu clusters are presented in Appendix A.5 (see Figure A.4, Table A.3 and Table A.4).

3.3.4 CO adsorption over Ni_{n+1} and Ni_nCu clusters ($1 \leq n \leq 12$)

The CO adsorption was done on each cluster (presented in Figure 3.1) followed by complete geometrical relaxation. For the adsorption (depending upon the structural geometry and availability of sites), three sites were considered viz. bridge, hollow, and top sites with the carbon (C) end-on mode as shown in the schematic of Figure 3.6(a). The side-on configuration will be discussed later. The adsorption energy of CO onto Ni_{n+1} and Ni_nCu clusters is defined

$$E_{(CO-ads)} = E_{[cluster+(CO)]} - E_{(cluster)} - E_{(CO)} \qquad (3.5)$$

where $E_{[cluster+(CO)]}$, $E_{(cluster)}$, and $E_{(CO)}$ are the energy of the cluster adsorbed with CO, the bare cluster, and the CO molecule respectively.

The search of the most promising adsorption site onto Ni_{n+1} and Ni_nCu clusters was examined with the treatment of dispersive forces (D2 and D3) incorporated with the LDA and GGA functionals, and the energy value for the most preferable adsorption site is presented in Table 3.2. The energy value for other CO adsorption sites over Ni_{n+1} and Ni_nCu clusters is provided in Table A.5 and Table A.6 of Appendix A.6 respectively. On account of dispersion correction, similarity in results is detected between the two approaches, i.e., PBE and PBE-D3, with the ability to reproduce the experimentally observed preferred site (top site). The fully relaxed systems of CO adsorbed clusters with the most active site obtained with the PBE-D3 method are presented in Figure 3.6(b-c). The relevant distance between Ni−CO (R_{Ni-C}) and C−O (R_{C-O}) examined with the PBE + D3 approach is also presented in Table 3.2. It is noticed that the CO prefers to bind over the Ni atom with the C-end-on mode.
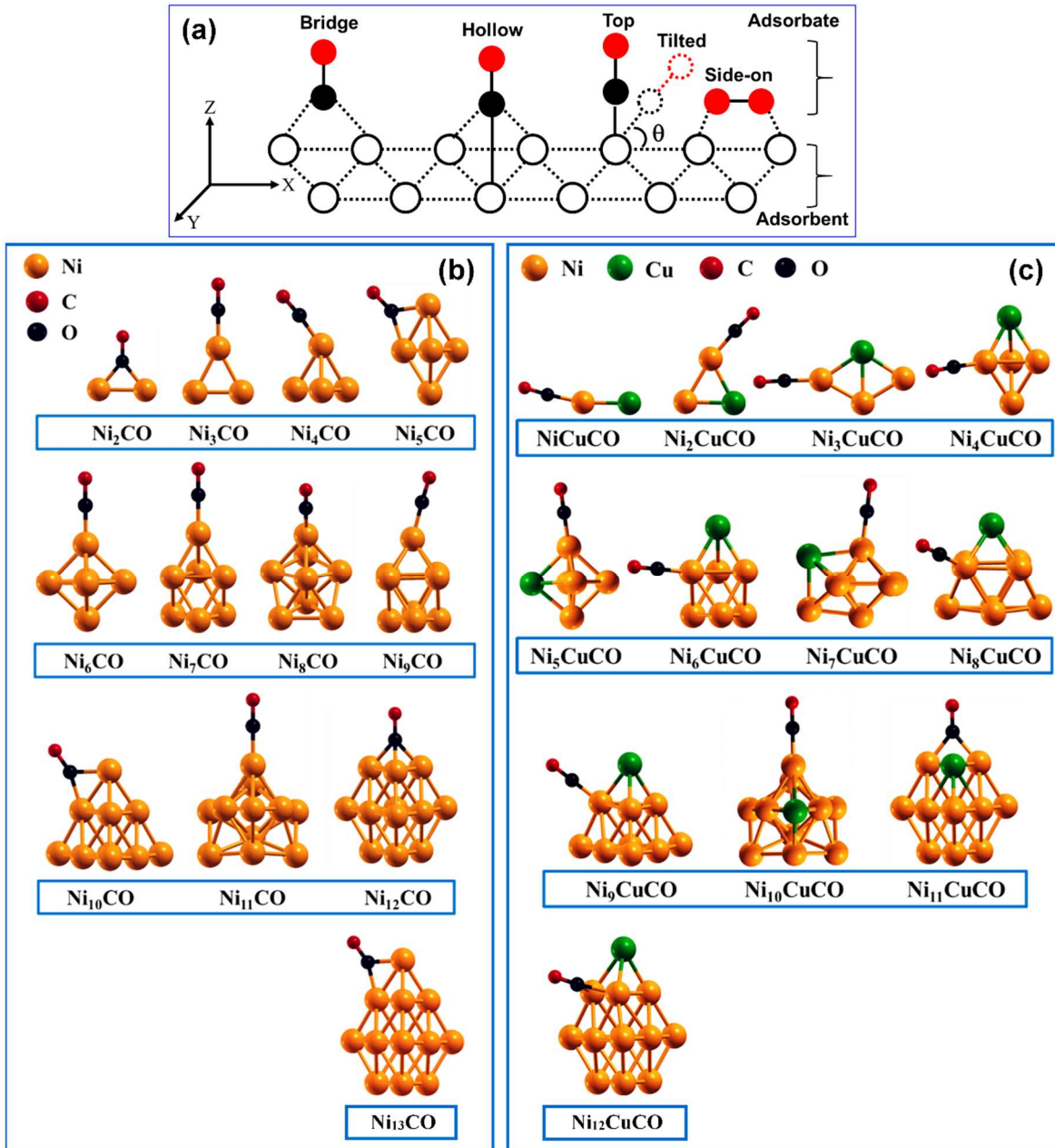
Figure 3.6: (a) Schematic orientation for the adsorbate (in x, y, and z axis) onto the adsorbent in four reference positions, i.e., bridge (parallel to the xz plane), hollow (perpendicular to the xy plane and parallel to the z axis), top (aligned parallel to the z direction), and side-on (parallel to the xz plane). The tilted orientation shows the deviation of adsorbate state after complete relaxation in some cases. In some cases, the adsorbate deviates from top to tilted orientation at a certain angle (θ) after complete relaxation. Lowest energy structures of (b) $Ni_{n+1}CO$ and (c) Ni_nCuCO systems.

Table 3.2: The adsorption energy ($E_{co\text{-}ads}$ eV) of CO over Ni_{n+1} and Ni_nCu clusters (calculated with various functional schemes), Ni–C ($R_{Ni\text{-}C}$ (Å)) and C–O ($R_{C\text{-}O}$ (Å)) bond distance, vibrational stretching frequency of CO molecule ($\upsilon_{C\text{-}O}$ (cm^{-1})). The H, B, and T characters indicate hollow, bridge, and top sites.

System	$E_{co\text{-}ads}$					$R_{Ni\text{-}C}$	$R_{C\text{-}O}$	$\upsilon_{C\text{-}O}$
	LDA	LDA-D2	PBE	PBE-D2	PBE-D3	PBE-D3		PBE-D3
Ni_2-CO	-3.09 (B)	-3.11 (B)	-2.16 (B)	-2.29 (B)	-2.27 (B)	1.77	1.20	1706
Ni_3-CO	-2.85 (B)	-2.91 (B)	-2.23 (T)	-2.27 (T)	-2.25 (T)	1.74	1.16	1937
Ni_4-CO	-3.09 (H)	-3.19 (H)	-2.23 (T)	-2.30 (T)	-2.27 (T)	1.73	1.17	1930
Ni_5-CO	-3.00 (H)	-3.16 (H)	-2.22 (B)	-2.31 (B)	-2.26 (B)	1.72	1.17	1930
Ni_6-CO	-2.91 (H)	-3.21 (H)	-2.09 (T)	-2.16 (T)	-2.14 (T)	1.71	1.17	1915
Ni_7-CO	-2.69 (H)	-3.06 (H)	-1.84 (T)	-1.90 (B)	-1.88 (T)	1.75	1.16	1915
Ni_8-CO	-2.70 (H)	-3.19 (H)	-1.95 (T)	-2.02 (T)	-2.00 (T)	1.74	1.16	1957
Ni_9-CO	-2.73 (H)	-3.19 (B)	-1.92 (T)	-1.98 (T)	-1.96 (T)	1.74	1.16	1923
Ni_{10}-CO	-2.58 (H)	-3.29 (H)	-1.69 (T)	-1.80 (H)	-1.74 (B)	1.76	1.16	1988
Ni_{11}-CO	-2.66 (H)	-3.52 (H)	-1.92 (T)	-1.98 (T)	-1.95 (T)	1.74	1.16	1902
Ni_{12}-CO	-3.06 (H)	-4.09 (H)	-2.24 (H)	-2.37 (H)	-2.31 (H)	1.93	1.20	1657
Ni_{13}-CO	-2.70 (H)	-2.86 (H)	-1.94 (B)	-2.05 (B)	-2.00 (B)	1.88	1.18	1796
NiCu-CO	-2.36 (T)	-2.39 (T)	-1.98 (T)	-2.05 (T)	-2.05 (T)	1.75	1.16	1956
Ni_2Cu-CO	-3.19 (B)	-3.24 (B)	-2.46 (T)	-2.46 (T)	-2.43 (T)	1.72	1.17	1882
Ni_3Cu-CO	-2.52 (T)	-2.60 (T)	-1.93 (T)	-1.98 (T)	-1.96 (T)	1.73	1.16	1941
Ni_4Cu-CO	-2.78 (B)	-2.89 (B)	-2.22 (T)	-2.37 (T)	-2.27 (T)	1.73	1.16	1934
Ni_5Cu-CO	-2.76 (T)	-2.85 (T)	-2.01 (T)	-2.11 (T)	-2.08 (T)	1.72	1.16	1943
Ni_6Cu-CO	-2.83 (T)	-2.95 (T)	-2.09 (T)	-2.19 (T)	-2.16 (T)	1.72	1.16	1939
Ni_7Cu-CO	-2.62 (T)	-2.75 (T)	-1.85 (T)	-1.97 (T)	-1.92 (T)	1.72	1.17	1935
Ni_8Cu-CO	-2.44 (T)	-2.59 (T)	-1.78 (T)	-1.87 (T)	-1.86 (T)	1.74	1.17	1917
Ni_9Cu-CO	-2.30 (T)	-2.42 (T)	-1.80 (T)	-1.92 (T)	-1.87 (T)	1.74	1.17	1939
Ni_{10}Cu-CO	-2.41 (T)	-2.49 (T)	-1.90 (T)	-1.94 (T)	-1.94 (T)	1.75	1.16	1968
Ni_{11}Cu-CO	-2.90 (H)	-3.01 (H)	-2.18 (B)	-2.30 (B)	-2.25 (B)	1.86	1.19	1782
Ni_{12}Cu-CO	-2.33 (H)	-2.48 (H)	-1.59 (B)	-1.87 (B)	-1.68 (B)	1.88	1.19	1734

The calculated (experimental Ref. [57]) bond-length (C –O) and vibrational frequency ($\upsilon_{C\text{-}O}$) of CO gas molecule are 1.14 Å (1.13 Å) and 2125 cm^{-1} (2170 cm^{-1}).

The variation examined in the CO adsorption energy and site preference (most preferable) for Ni$_{n+1}$ and Ni$_n$Cu clusters with LDA and PBE functionals alone and along with the dispersive forces, i.e., D2 and D3 are discussed here in detail. For the Ni$_{n+1}$ clusters with the LDA functional, CO prefers a hollow site except for Ni$_2$ and Ni$_3$ clusters. Even after the incorporation of D2 with the LDA functional, site preference remains the same except for Ni$_9$ cluster. With the PBE functional, the bridge site is preferred by the Ni$_2$, Ni$_5$, and Ni$_{13}$ clusters, and the rest of the clusters favored the top site for the CO adsorption. It is evident from Table 3.2 that the site ordering is very much divergent with the appearance of D2 whereas the highly accurate D3 appears to trap CO onto a top site i.e., very much similar to the PBE functional. As the accuracy of the correction (D3) increases, the bridge site becomes competitive and eventually turns out to be the lowest energy site for the Ni$_{10}$ cluster. Inspection of Table 3.2 indicates that the LDA functional with dispersion correction (D2) fails to reproduce the experimentally observed preference for the top site, while PBE functional with higher accuracy correction (D3) seems capable to predict the correct adsorption site (top site) except for few Ni$_{n+1}$ clusters. In the case of Ni$_n$Cu clusters, the CO molecule desires to react with the nearest Ni atom (i.e., close to the Cu atom is defined as the nearest Ni atom) as compared to other Ni atoms. For a particular size, the adsorption energy of CO over Ni$_n$Cu clusters decreases, proposing that the introduction of the Cu atom reduces the adsorption ability (display inertness) of CO molecule on the cluster as predicted in the earlier reports [10,12]. The site preference for CO adsorption is found similar for the LDA and LDA+D2 calculations with improved consistency to reproduce experimentally preferred top site only for several Ni$_n$Cu clusters (see Table 3.2). For ease of understanding, the conditions/factors affecting the (increment/decrement/no-change) adsorption trend and CO adsorption energy examined with PBE+D3 calculations are provided and explained in Table 3.3. For comparison, the adsorption energy ($E_{(CO\text{-}ads)}$) of CO for the favorable site on the Ni$_{n+1}$ and Ni$_n$Cu clusters is presented in the heatmap of Figure 3.7(a-b).

Table 3.3: Analysis of conditions/factors affecting the magnitude adsorption energy and adsorption trend of CO over $Ni_n Cu$ clusters examined with PBE+D3 calculations.

| Systems	Löwdin charge analysis Charge transfer (e) before CO adsorption		Effect on Cu atom	Effect on Ni atom	Adsorption Energy Trend	Switching of Site after Cu doping
	Cu to Ni	Ni to Cu				
NiCu	-	0.02	-	deficient of charge	Decrease	bridge to top
Ni_2Cu	0.01	-	deficient of charge	-	Increase	top(straight)-top (slightly tilted towards Cu)
Ni_3Cu	-	0.08	-	deficient of charge	Decrease	top(tilted) to top(straight)
Ni_4Cu	0.11	-	deficient of charge	-	No change	bridge to top (nearest Ni atom)
Ni_5Cu	0.02	-	deficient of charge	-	Decrease	top to top (nearest Ni atom)
Ni_6Cu	0.12	-	deficient of charge	-	Increase	top to top (highly co-ordinated nearest Ni atom)
Ni_7Cu	0.12	-	deficient of charge	-	Decrease	top to top (highly co-ordinated nearest Ni atom)
Ni_8Cu	0.14	-	deficient of charge	-	Decrease	top (slightly tilted) to top (straight and highly co-ordinated nearest Ni atom)
Ni_9Cu	0.22	-	deficient of charge	-	Increase	bridge to top (highly co-ordinated nearest Ni atom)
$Ni_{10}Cu$	0.19	-	deficient of charge	-	No change	top to top (position not changed)
$Ni_{11}Cu$	0.11	-	deficient of charge	-	Decrease	hollow to bridge (nearest Ni atoms)
$Ni_{12}Cu$	0.11	-	deficient of charge	-	No change	top to top (position not changed)
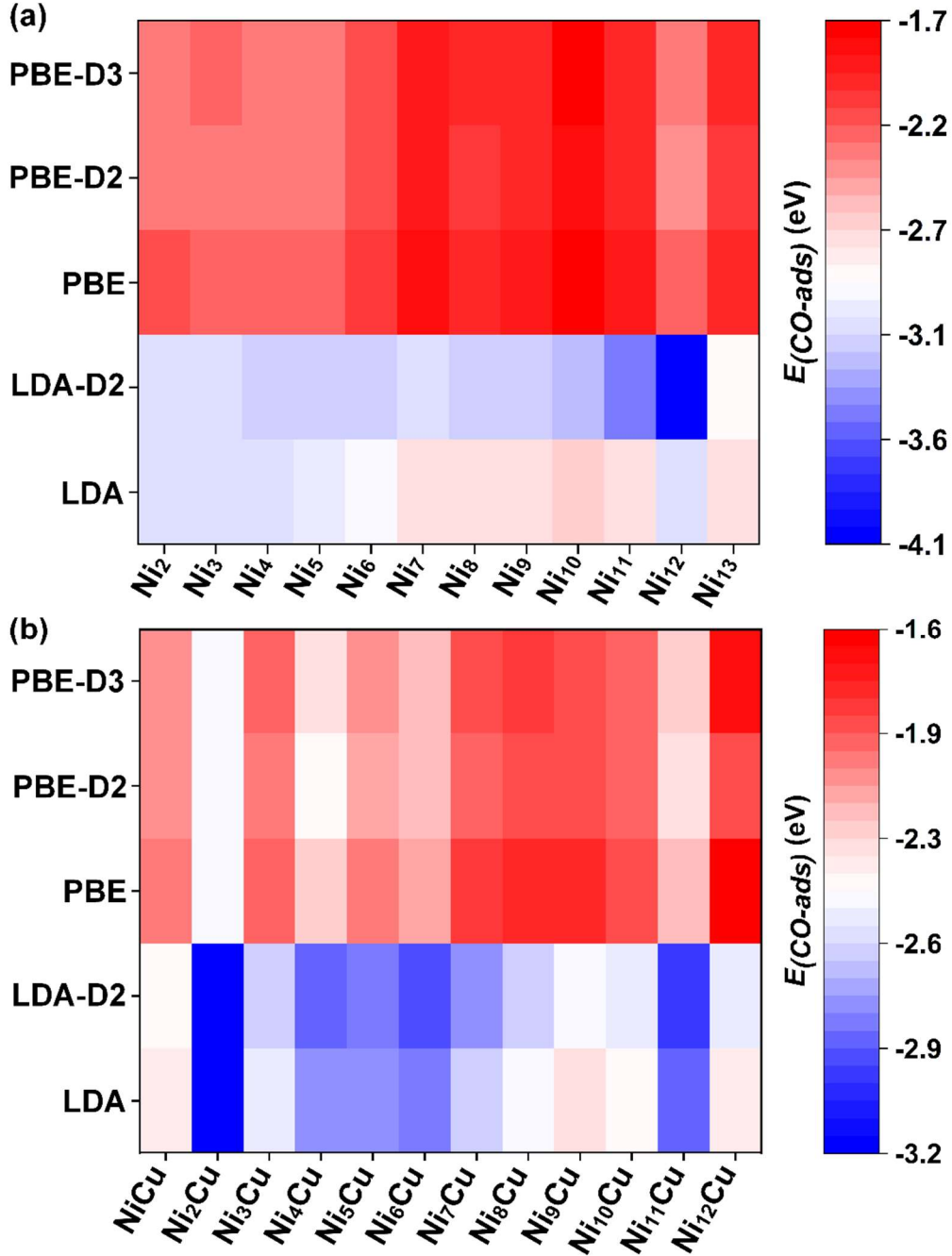
Figure 3.7: Heatmap of CO adsorption energy ($E_{CO\text{-}ads}$ eV) over (a) Ni$_{n+1}$ and (b) Ni$_n$Cu clusters with respect to different functionals and their combination with dispersion corrections (D2 and D3).

We can see that the value of E$_{(CO\text{-}ads)}$ alters with the type of functional as well as with the incorporation of D2 and D3 corrections. For the LDA and LDA+D2 calculations, E$_{(CO\text{-}ads)}$ tends to have high negative values, while the low negative values are inspected for the PBE functional with and without incorporation of D2 and D3 corrections. These results are consistent with the previous study reported on CO

interaction with $Cu(HCOO)_2$ cluster model [56]. The properties of the CO gas molecule obtained with the PBE-D3 scheme are summarized and compared with experimental data in Table 3.2 [57]. Prior to the above discussion, we would like to address the vibrational stretching frequency ($\upsilon_{C-O}\,cm^{-1}$) of CO for the most active site on Ni_{n+1} and Ni_nCu clusters which is presented in Table 3.2. One can easily observe from Table 3.2 that υ_{C-O} is very sensitive to Ni–CO bond strength and C–O bond length. Therefore, the variation observed in υ_{C-O} after CO adsorption over the Ni_{n+1} and Ni_nCu clusters is compared with lengthening/shortening of C–O bond length and is discussed pointwise. (1) For Ni_nCu clusters where n = 2, 7, 8, 9, and 12, lengthening of the C–O bond resulted in the lower υ_{C-O} as compared to respective Ni_{n+1} clusters and (2) for the rest of the Ni_nCu clusters, the C–O bond shortened a little bit and hence causes the higher υ_{C-O} as compared to respective Ni_{n+1} clusters. From the prior analysis of relative energetic stabilities (especially the mixing energy), Ni_9, Ni_{13}, Ni_8Cu, and $Ni_{12}Cu$ clusters are considered as representative systems for further investigation, discussion and to perform CO oxidation reaction with the PBE-D3 approach.

3.3.5 Electronic properties

This section emphasizes the analysis of the spin-polarized density of states (DOS) projected onto the Ni 3d orbitals of Ni_9 and Ni_{13} clusters and simultaneously the spin-polarized DOS projected onto the 3d orbitals of Ni and Cu atoms of Ni_8Cu and $Ni_{12}Cu$ clusters and are presented in Figure. 3.8(a-d). The electronic reactivity descriptors of Ni_9 and Ni_{13}, Ni_8Cu and $Ni_{12}Cu$ clusters are calculated using equation (3-6) [37-38] and is presented in Table 3.4. The band of d-states participating in the interaction approximated with single state energy about the Fermi level is called the *d-band* center (ε_d). According to the conventional *d-band* model, the lower(upward) shift of ε_d indicates the less(higher) availability of empty antibonding states resulted in the weaker(stronger) affinity of transition metals (TM) towards adsorbate. In this study, spin-polarization is considered throughout the calculation. Thus, two *d-band* centers (1)

for the spin-up states ($\varepsilon_{d\uparrow}$) and (2) for the spin-down states ($\varepsilon_{d\downarrow}$) are computed. The numbers depicted in Table 3.4 imply that the attractive interaction mainly arises from the $\varepsilon_{d\downarrow}$ (close to the EF), since it is unoccupied, while $\varepsilon_{d\uparrow}$ owes both attractive plus repulsive contributions mainly because of the $f_{l\uparrow} > f_{l\downarrow}$ (see Table 3.4 for more details). Thus, for minority spin, *d-band* binds more strongly to the adsorbate, while the binding with majority spin is weaker. In the case of Ni$_9$ and Ni$_{13}$ clusters, the position of $\varepsilon_{d\downarrow}$ (almost identical) is closer to the E$_F$ than $\varepsilon_{d\uparrow}$ confirming more unoccupancy of antibonding states which causes the strong attractive interaction with the adsorbate. Going from the Ni$_9$ to the Ni$_{13}$ cluster, the upward shifting of $\varepsilon_{d\uparrow}$ offers more unoccupied states for CO adsorption (weaker repulsion for CO interaction compared to Ni$_9$ cluster). Hence, higher adsorption energy was observed for CO over Ni$_{13}$ cluster. In Ni$_8$Cu and Ni$_{12}$Cu clusters, the $\varepsilon_{d\downarrow}$ (or $\varepsilon_{d\uparrow}$) of Ni (more unoccupied states are available) is close to the E$_F$ than that for Cu atom, and thus CO prefers to be adsorbed over the nearest Ni atom of clusters. It seems that the degree of spin-polarization of Cu is smaller and therefore, the value of $\varepsilon_{d\downarrow}$ and $\varepsilon_{d\uparrow}$ are very much close to each other as shown in Table 3.4. Also, their activity seems similar since $f_{l\uparrow} \cong f_{l\downarrow}$. In comparison to Ni$_8$Cu cluster, negligible variation is observed in a position of the $\varepsilon_{d\uparrow}$ (Ni), while the $\varepsilon_{d\downarrow}$ of Ni is pulled down (availability of unoccupied states is lesser) leading to the strong repulsion with CO in the case of Ni$_{12}$Cu cluster and is consistent with the obtained adsorption trend. It is important to point out that the fractional filling $f_{l\uparrow}$ and $f_{l\downarrow}$ of Ni, *d-band* remains constant (with a little bit of variation) for pure and Cu coped Ni clusters. Hence, each metal system has to compensate for variations in the width by shifting the d-states up or down in energy depending on the nature of the variation. The $W_{d\uparrow}$ and $W_{d\downarrow}$ varies significantly with the coordination number of the system. Generally, the amount of overlap between interatomic matrix elements of neighboring atoms of Ni$_9$, Ni$_{13}$, Ni$_8$Cu, and Ni$_{12}$Cu clusters is quantified by the W_d (the second central moment of the d-DOS) and its value is depicted in Table 3.4.
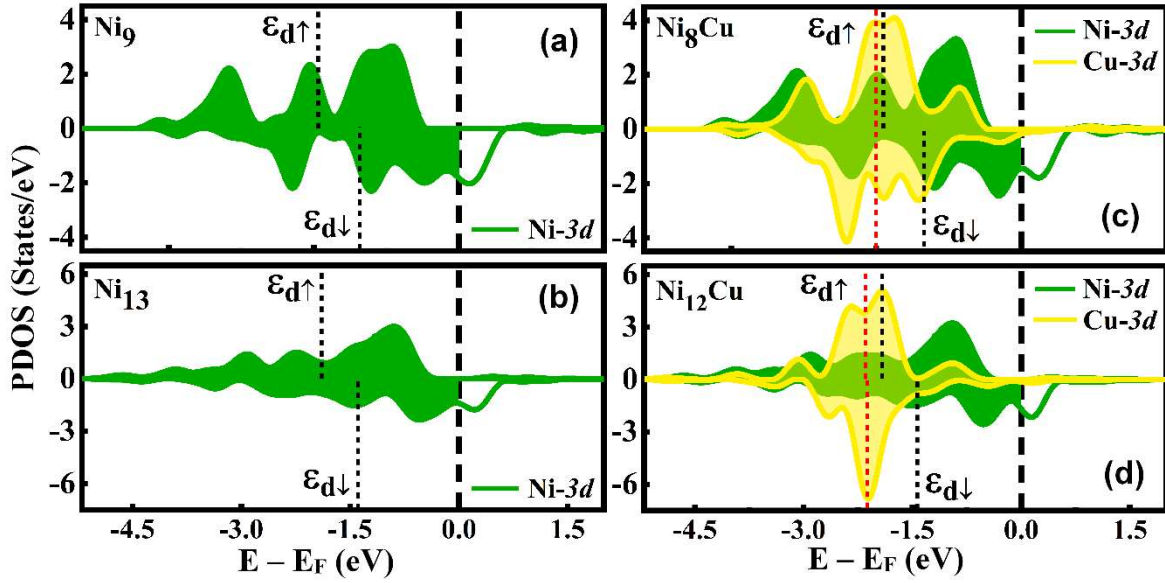
Figure 3.8: The spin-polarized projected density of states (PDOS) of (a) Ni_9, (b) Ni_{13}, (c) Ni_8Cu, and (d) $Ni_{12}Cu$ clusters. The short dash line in black and red color represents the *d-band* center of Ni and Cu respectively for spin-up and spin-down state. The long dash line at zero indicates the Fermi energy. The filled and unfilled regions represent the bonding and anti-bonding states, respectively.

Moving from Ni_9 (ECN = 4.67) to Ni_{13} (ECN = 5.46) cluster, $W_{d\uparrow}$ and $W_{d\downarrow}$ broadened as the value of ECN increases. A similar tendency is displayed by $W_{d\uparrow}$ and $W_{d\downarrow}$ of Ni for the Ni_8Cu and $Ni_{12}Cu$ clusters. A quite reverse trend is investigated for $W_{d\uparrow}$ and $W_{d\downarrow}$ of Cu that is attributed by the alteration in the position of Cu atom from higher coordinated site to lower coordinated site (3d orbitals of neighboring atoms become more contracted). One can visualize this by comparing the PDOS plot of Ni_8Cu and $Ni_{12}Cu$ clusters, where the Cu 3d orbitals contract and shift down. Thus $W_{d\uparrow}$ and $W_{d\downarrow}$ gets narrower which results in downshifting of the $\varepsilon_{d\downarrow}$ and $\varepsilon_{d\uparrow}$ as we move from Ni_8Cu to $Ni_{12}Cu$ clusters. These "electronic reactivity descriptors" derived from the improved *d-band* model are crucial to elucidate the CO-poisoning free reactivity of Ni-catalyst. We analyzed the underlying mechanism of degrading adsorption of CO after Cu doping. For this, the spin-polarized DOS and labeled orbitals of a free CO molecule along with the PDOS of Ni_9CO, $Ni_{13}CO$, Ni_8CuCO, and $Ni_{12}CuCO$ systems are illustrated in Figure 3.9(a-e).
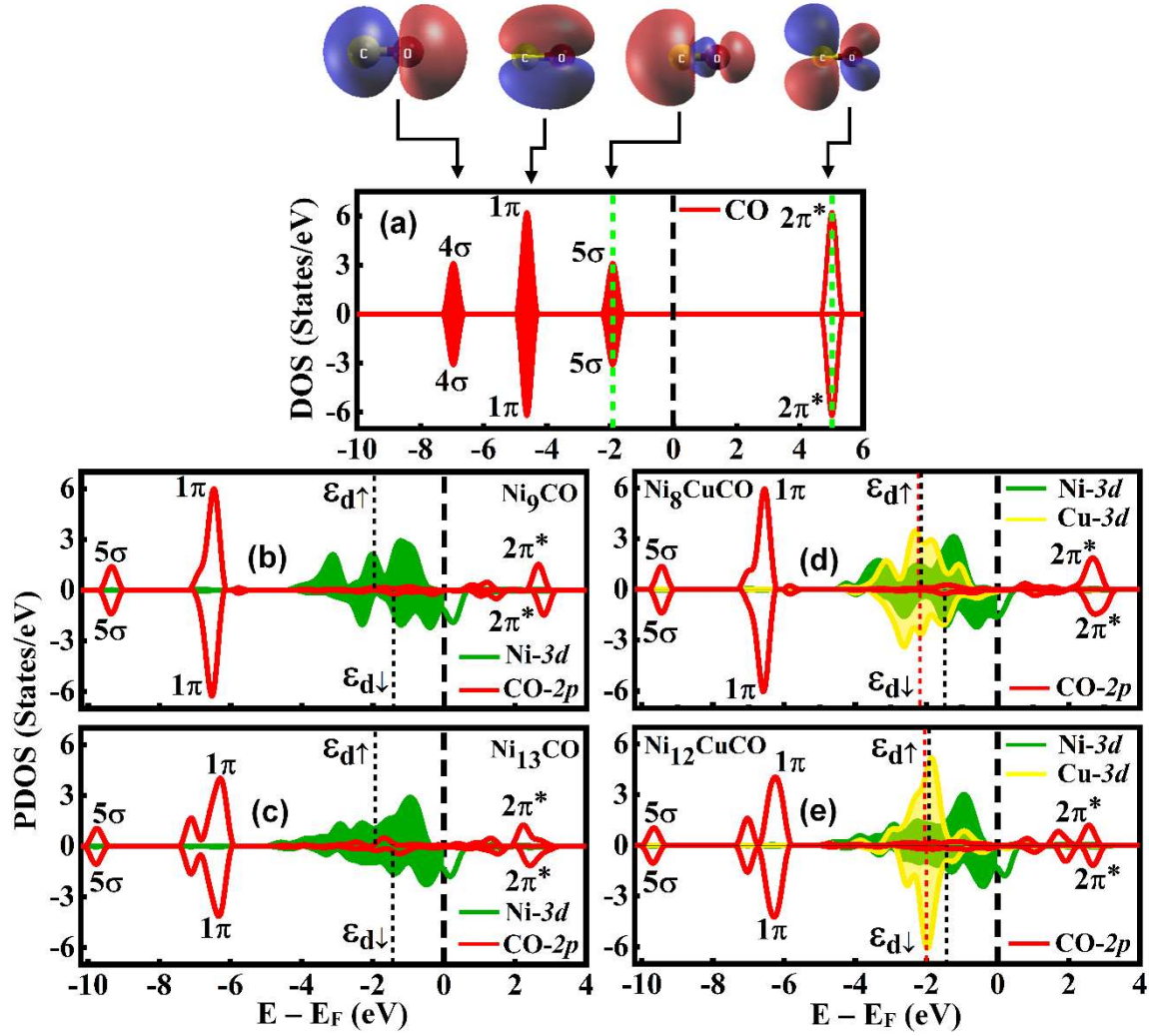
Figure 3.9: (a) The spin-polarized density of states of CO molecule and labeled orbitals. The spin-polarized projected density of states of (b) Ni$_9$CO, (c) Ni$_{13}$CO, (d) Ni$_8$CuCO and (e) Ni$_{12}$CuCO systems. The green dash line indicates the HOMO and LUMO state of the CO molecule. The short dash line in black and red color represents the *d-band* center of Ni and Cu respectively. The long dash line at zero indicates the Fermi energy. The filled and unfilled regions for the metals represent the bonding and anti-bonding states, respectively.

For the isolated CO molecule, 4σ comes from the O lone pairs, 5σ is contributed by the C lone pairs, and 1π and 2π* (fully empty since it is located far above Fermi level) appear from the bonding and antibonding states of CO [58]. It can be seen from Figure 3.9(b-e) that the 1π and 5σ orbitals of CO are in inverse order relative to its gas phase. Primarily, the adsorption of CO over representative clusters is mainly governed by the π-back donation of electrons from Ni 3d orbitals to the empty 2π* orbitals

(LUMO) of CO which initiates the broadening of the $2\pi^*$ orbitals and is dragged down near the E$_F$. The PDOS presented in Figure 3.9(b-e) confirms the partial filling of $2\pi^*$ orbitals of CO which leads to the elongation of the C−O bond (see Table 3.2 for more information). Second, the repulsive interaction between the 5σ orbitals (HOMO) of CO and filled Ni 3d orbitals strengthens the bonding of the Ni−CO system, which results in the downshifting of 5σ orbitals far from Fermi level when compared with the DOS of CO molecule. In general, increment (decrement) in repulsion between the occupied 5σ orbitals of CO and the filled 3d orbitals of Ni atom strengthens (weakens) the Ni-CO interaction which ultimately leads to the weakening (strengthening) of the C−O bond. Correspondingly, a smaller (higher) vibrational stretching frequency was detected for the CO molecule as compared to its gas phase (see Table 3.2 for more detail). These findings are consistent with the model proposed by Bagus et al. [59] that suggested π-back-donation and σ-repulsion for a metal−carbonyl bond. Figure 3.9(d-e) reflects the downshifting of Ni 3d orbitals in comparison to Ni$_9$CO and Ni$_{13}$CO systems, confirming the decrement in the energy of the bonding states. Apparently, the overlap of CO $2\pi^*$ states with Ni 3d orbitals (lower availability of 3d states due to charge transfer from Cu to Ni) is lighter in Cu doped systems and is responsible for the weaker interaction of CO relative to the pure Ni clusters. To support these results effective Löwdin charge on each atom is analyzed through $Q_{eff} = Z_V − Q_{Löwdin}$, where Z_V is the valence charge and $Q_{Löwdin}$ is the Löwdin charge. The spin-dependent effective Löwdin charge discriminated for clusters along with the C and O atoms of CO molecule for Ni$_{n+1}$CO and Ni$_n$CuCO systems are depicted in Table 3.5 and Table 3.6, respectively which indicate an electron donation from C atom to the cluster (except for few cases), while the O atom gains charge as a consequence of electron back-donation by the cluster, which is consistent with the well-known donation-back-donation process used to rationalize the interaction of CO and NO with TM substrates [59-60]. The effective Löwdin charge analysis also confirms that the net charge is transferred from the CO molecule to the cluster.

To rationalize the electronic structure of clusters with adsorbed CO molecule, the charge density distributions in the HOMO ($\uparrow$ and $\downarrow$) and LUMO ($\uparrow$ and $\downarrow$) states of Ni$_9$CO, Ni$_{13}$CO, Ni$_8$CuCO, and Ni$_{12}$CuCO systems are demonstrated in Figure 3.10(a-b). One can visualize a π-like bond between the Ni atom and C atom in the LUMO state (empty $2\pi^*$ orbitals), i.e., pulled down near to the E$_F$. As a result, the CO molecule is activated by the elongation of the C–O bond length as compared to its gas phase.

Table 3.4: Calculated *d-band* center (ε_d, eV), *d-band* filling (f_l, eV), and *d-band* widths (W_d, eV) for both the spin-up and the spin-down states of the representative cluster systems.

System	*d-band* center				*d-band* filling				*d-band* width			
	$\varepsilon_{d\uparrow}$	$\varepsilon_{d\downarrow}$	$\varepsilon_{d\uparrow}$	$\varepsilon_{d\downarrow}$	$f_{l\uparrow}$	$f_{l\downarrow}$	$f_{l\uparrow}$	$f_{l\downarrow}$	$W_{d\uparrow}$	$W_{d\downarrow}$	$W_{d\uparrow}$	$W_{d\downarrow}$
	Ni	Ni	Cu	Cu	Ni	Ni	Cu	Cu	Ni	Ni	Cu	Cu
Ni$_9$	-1.94	-1.37	-	-	0.9849	0.8031	-	-	1.00	0.94	-	-
Ni$_{13}$	-1.89	-1.39	-	-	0.9787	0.8135	-	-	1.10	1.07	-	-
Ni$_8$Cu	-1.90	-1.34	-2.00	-2.00	0.9828	0.8071	0.9879	0.9825	1.01	0.96	0.53	0.54
Ni$_{12}$Cu	-1.92	-1.43	-2.15	-2.12	0.9770	0.8180	0.9879	0.9771	1.11	1.10	0.42	0.39

Table 3.5: The spin-dependent effective Löwdin charge analysis of Ni$_{n+1}$CO systems. The Δq^X (where X = C, O, CL(cluster)) is the effective Löwdin charge on the corresponding X atom/cluster, for which $\Delta q > 0$ means loss of charge while $\Delta q < 0$ is the gain of charge.

System	$\Delta q^C(\uparrow)$	$\Delta q^C(\downarrow)$	$\Delta q^O(\uparrow)$	$\Delta q^O(\downarrow)$	$\Delta q^{CL}(\uparrow)$	$\Delta q^{CL}(\downarrow)$
Ni$_2$	-0.01	-0.02	-0.06	-0.07	1.01	-0.91
Ni$_3$	0.06	0.02	-0.02	-0.03	0.04	-0.14
Ni$_4$	0.05	0.03	-0.03	-0.03	0.56	-0.64
Ni$_5$	0.05	0.04	-0.03	-0.03	0.36	-0.44
Ni$_6$	0.07	0.03	-0.03	-0.04	0.87	-0.97
Ni$_7$	0.04	0.04	-0.01	-0.03	-0.09	-0.009
Ni$_8$	0.05	0.04	-0.01	-0.04	-0.08	-0.02
Ni$_9$	0.05	0.04	-0.008	-0.04	-0.07	-0.03
Ni$_{10}$	0.05	0.03	-0.009	-0.03	-0.08	-0.03
Ni$_{11}$	0.05	0.03	-0.01	-0.03	-0.07	-0.03
Ni$_{12}$	-0.01	-0.07	-0.004	-0.08	0.04	0.04
Ni$_{13}$	0.02	-0.006	-0.02	-0.05	0.10	-0.12

Table 3.6: The spin-dependent effective Löwdin charge analysis of Ni_nCuCO systems. The Δq^X (where X = C, O, CL(cluster)) is the effective Löwdin charge on the corresponding X atom/cluster, for which $\Delta q > 0$ means loss of charge while $\Delta q < 0$ is the gain of charge.

System	$\Delta q^C(\uparrow)$	$\Delta q^C(\downarrow)$	$\Delta q^O(\uparrow)$	$\Delta q^O(\downarrow)$	$\Delta q^{CL}(\uparrow)$	$\Delta q^{CL}(\downarrow)$
NiCu	0.05	0.03	-0.001	-0.02	-0.11	-0.03
Ni_2Cu	0.05	0.02	-0.02	-0.04	0.32	-0.39
Ni_3Cu	0.05	0.03	-0.03	-0.03	0.98	-1.04
Ni_4Cu	0.07	0.03	-0.02	-0.04	0.03	-0.12
Ni_5Cu	0.07	0.04	-0.03	-0.03	0.94	-1.05
Ni_6Cu	0.07	0.05	-0.03	-0.03	0.93	-1.04
Ni_7Cu	0.08	0.04	-0.02	-0.04	0.95	-1.06
Ni_8Cu	0.05	0.05	-0.02	-0.04	-0.04	-0.07
Ni_9Cu	0.05	0.05	-0.02	-0.04	-0.09	-0.01
$Ni_{10}Cu$	0.06	0.02	0.01	-0.009	-0.08	-0.05
$Ni_{11}Cu$	0.01	-0.02	-0.02	-0.06	0.03	-0.03
$Ni_{12}Cu$	0.02	0.006	-0.02	-0.06	-0.10	0.08

The charge transfer from the cluster to the CO molecule is expressed by the HOMO state that is contributed by the strong hybridization of the C 2p states and Ni 3d states. These observations imply that the CO molecule binds through the HOMO state of clusters, in which the adsorption mode would ensure maximum overlap of the orbitals which facilitates the charge donation from the cluster to the molecule. Further examination of the charge redistribution between Ni and C atoms in the HOMO state was found to be higher in the case of pure Ni clusters as compared to those for the Cu doped clusters. Based on the earlier discussion, the presence of an electrostatic interaction is recognized between the Ni and C atoms. The charge transfer from the Cu to the Ni atom weakens the Ni_nCu–CO interaction which initiates decrement in CO adsorption energy and may lead to the enhanced catalytic activity with degrading CO poisoning.
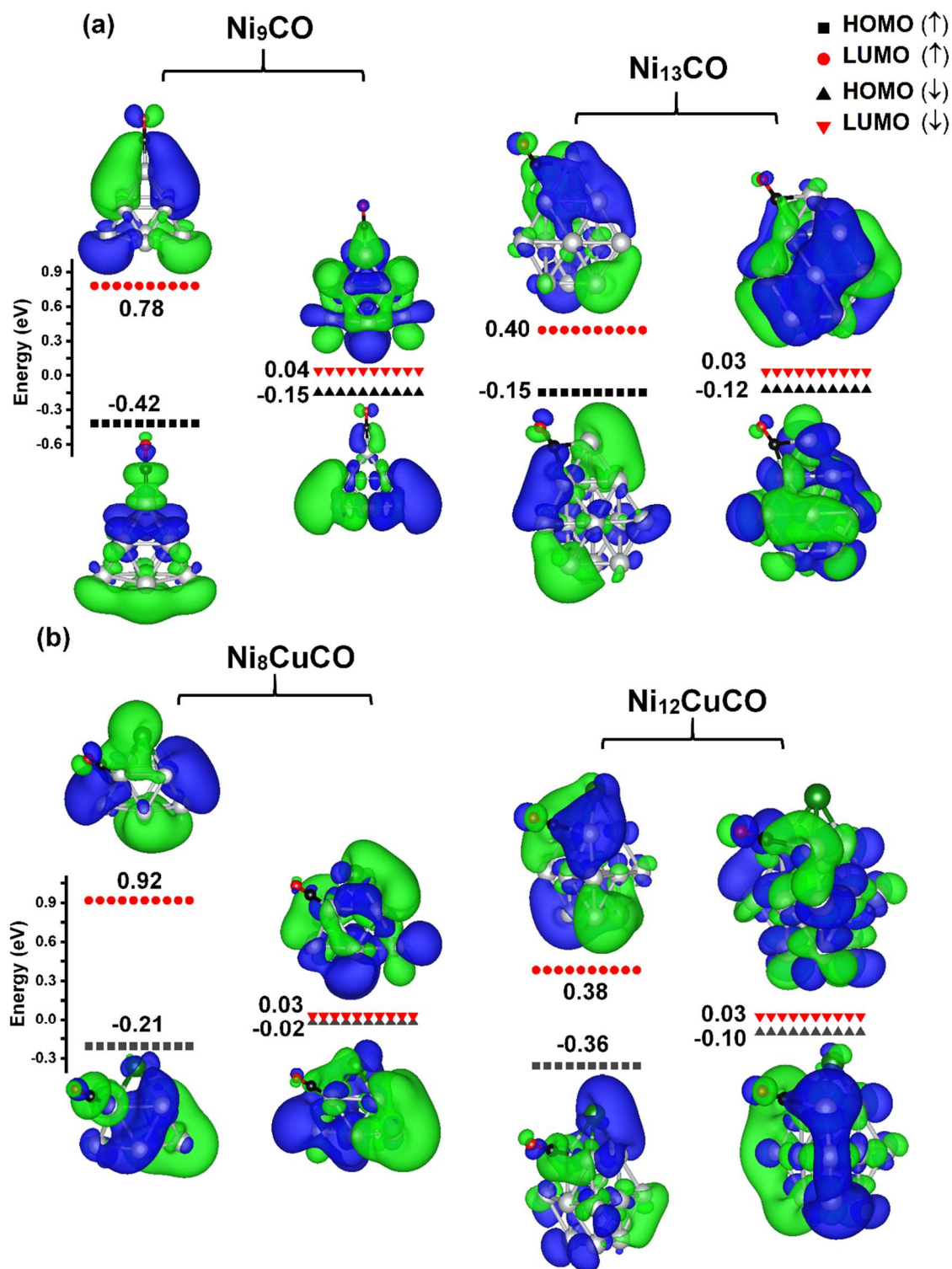
Figure 3.10: The molecular orbital of HOMO and LUMO state (for spin-up and spin-down) of (a) Ni$_9$CO and Ni$_{13}$CO systems and (b) Ni$_8$CuCO and Ni$_{12}$CuCO systems with an iso-surface value of ±0.0004 e/Å^3.

3.3.6 Charge density difference

To picturize the charge redistribution of molecular orbitals in CO adsorbed systems, we have analyzed and illustrated 3D iso-surface of Ni_9CO, $Ni_{13}CO$, Ni_8CuCO, and $Ni_{12}CuCO$ systems with average planar charge density differences ($\Delta\rho_z$) along the normal direction (z-axis) in Figure 3.11. At first glance, notable charge density redistribution was spotted out in the neighborhood of the adsorption site by the 3D iso-surfaces presented in Figure 3.11 since it is directly linked to the interaction between cluster and CO molecule. The charge transfer and polarization initiated this charge redistribution, i.e., ultimately relying on the hybridization of Ni 3d orbitals with 2p orbitals of CO molecule.
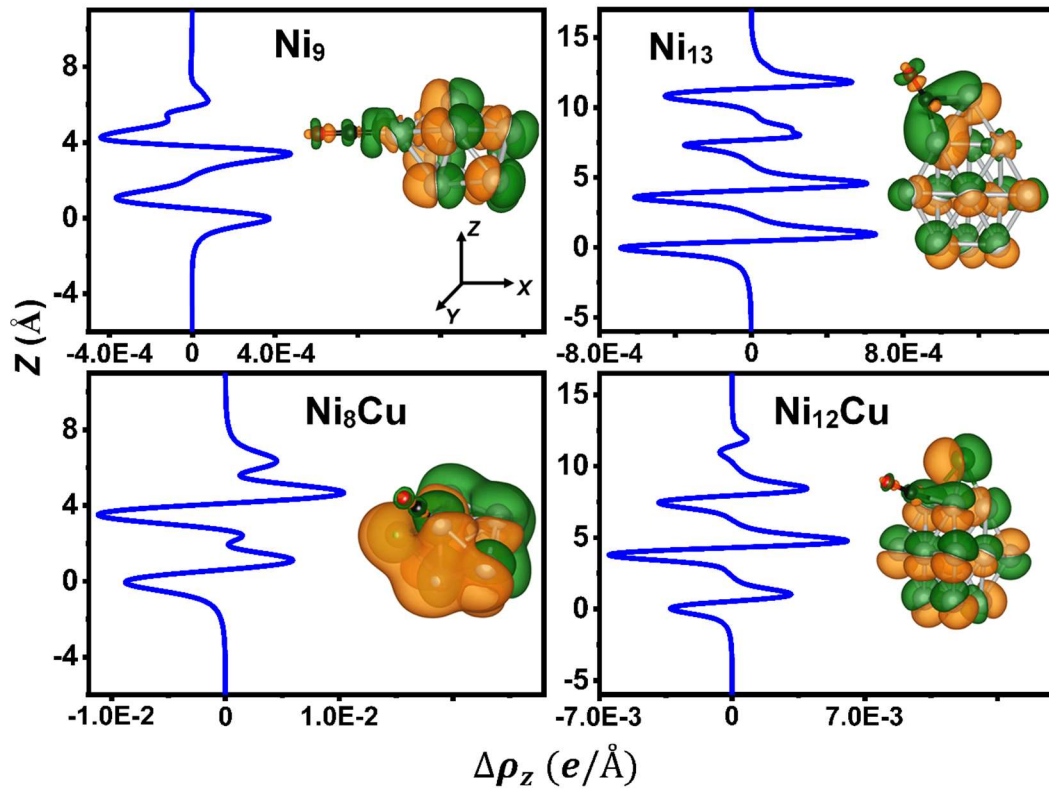

Figure 3.11: Charge density difference for CO adsorbed Ni_9, Ni_{13}, Ni_8Cu and $Ni_{12}Cu$ clusters. The orange (green) color represents the charge accumulation (depletion). The value of iso-surface is set to ± 0.005 e/Å^3 for Ni_9CO and $Ni_{13}CO$ systems. The value of iso-surface is set to ± 0.01 e/Å^3 for Ni_8CuCO and $Ni_{12}CuCO$ systems. The charge density difference is calculated using the formula $\Delta\rho = \rho_{(Cluster+gas/atom)} - \rho_{(Cluster)} - \rho_{(gas/atom)}$.

At the same time, a very minor redistribution of charge density was detected around atoms those are far from the adsorption site. Correspondingly, this fact reflects in the plot of the average planar charge density difference portrayed in Figure 3.11 for respective systems. The charge density redistribution shows a very minor perturbation around the Cu atom (the Cu 3d states are more localized) as compared to the Ni atom (bonded with CO molecule) which is endorsed by the stronger interaction of CO with the Ni atom. During the CO adsorption process, the $d_{xz}/d_{x^2-y^2}$ orbitals display a pronounced depletion, i.e., the source of back-donation from the Ni to the O atom of the CO molecule [61]. From the adsorbed CO molecule, a depletion originates from the p_x orbitals of the C atom with a polarization around the C atom. This is the root of electron donation from the C to the Ni atom. The charge accumulation is mainly located over the $Op_{z,y}(2\pi^*)$ states [60].

3.3.7 Work-function analysis

To quantify the trend of charge density redistribution, the work function change ($\Delta\Phi$) upon CO adsorption is evaluated with the help of the following expression,

$$\Delta\Phi \ = \ \Phi^{Cluster+CO} - \ \Phi^{Cluster} \tag{3.6}$$

where $\Phi^{Cluster+CO}$ and $\Phi^{Cluster}$ are work functions of the cluster + CO system and the cluster, respectively. The obtained $\Delta\Phi$ is presented in Figure. 3.12.

In general, $\Delta\Phi < 0$ indicates charge transfer from the cluster to the region between the surface and CO, while, $\Delta\Phi > 0$ indicates the less charge transfer from cluster to CO. As expected, $\Delta\Phi > 0$ observed from Figure 3.12 (except for Ni_2 and Ni_3Cu clusters) indicates the less charge transfer from cluster to CO i.e., the balanced charge density redistribution appears in the region between the surface and adsorbate due to the charge donation–back–donation process [60]. Also, $\Delta\Phi > 0$ meant for the inward-pointing surface dipole moment (the negative end is outside of the surface) induced by CO adsorption and is beneficial for the formation of electrophilic CO.
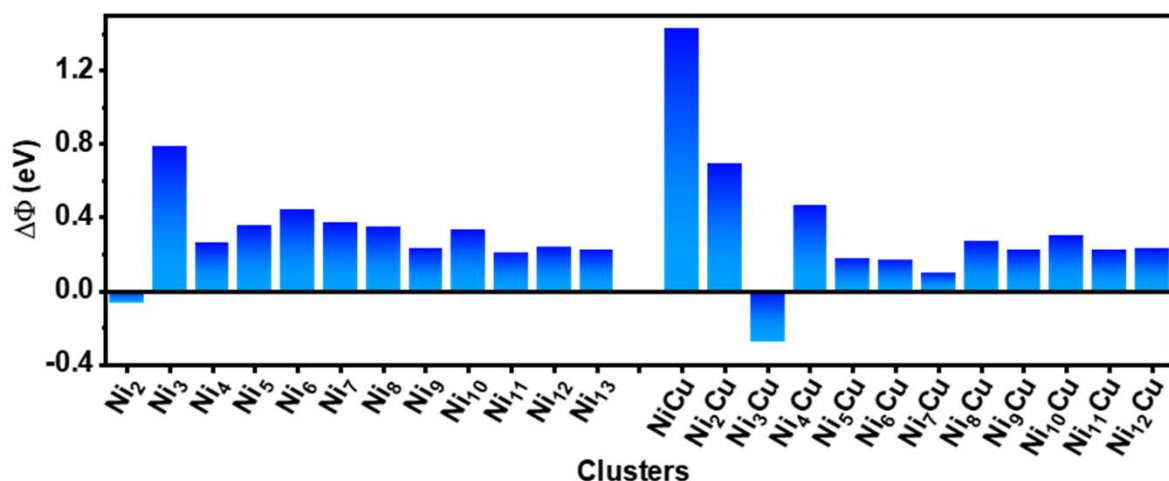
Figure 3.12: The change of work function $\Delta\Phi$ (eV) induced by CO adsorption over Ni$_{n+1}$ (left side) and Ni$_n$Cu (right side) clusters. The generalized formula to calculate work function for bare system or gas adsorbed system is $\Phi = E_{vac} - E_F$, where, E_{vac} is the energy of vacuum level of the system and E_F is the energy of Fermi level of the system.

This trend is consistent with the literature corresponding to the adsorption of a molecule with higher electronegativity as compared to substrate, which results in $\Delta\Phi > 0$ upon adsorption and introduces the accumulation of charge around molecule signifying a dipole pointing toward the surface. The highest positive value of $\Delta\Phi$ indicates accepting the least number of electrons and being most electrophilic. As shown in Figure 3.12, $\Delta\Phi < 0$ is found for Ni$_2$ and Ni$_3$Cu clusters upon the CO adsorption, and correspondingly the dipole moment pointing outward to the vacuum, which is led by the specific configuration of cluster and hybridization, despite overall charge transfer.

3.3.8 CO oxidation reaction pathway

It was vastly reported in earlier studies that the L-H mechanism is more promising for the CO oxidation reaction [10,62]. Therefore, we decided to proceed via the L-H mechanism which is divided into two half-reactions. (1) $CO + \frac{1}{2}O_2 \rightarrow CO_2$ (involves the splitting of the side-on superoxo bond/breaking of the Ni$-$O bond) and (2) $CO + O \rightarrow CO_2$ (the CO oxidation barrier depends on the breaking of the Ni$-$O bond) to perform CO oxidation over representative systems.
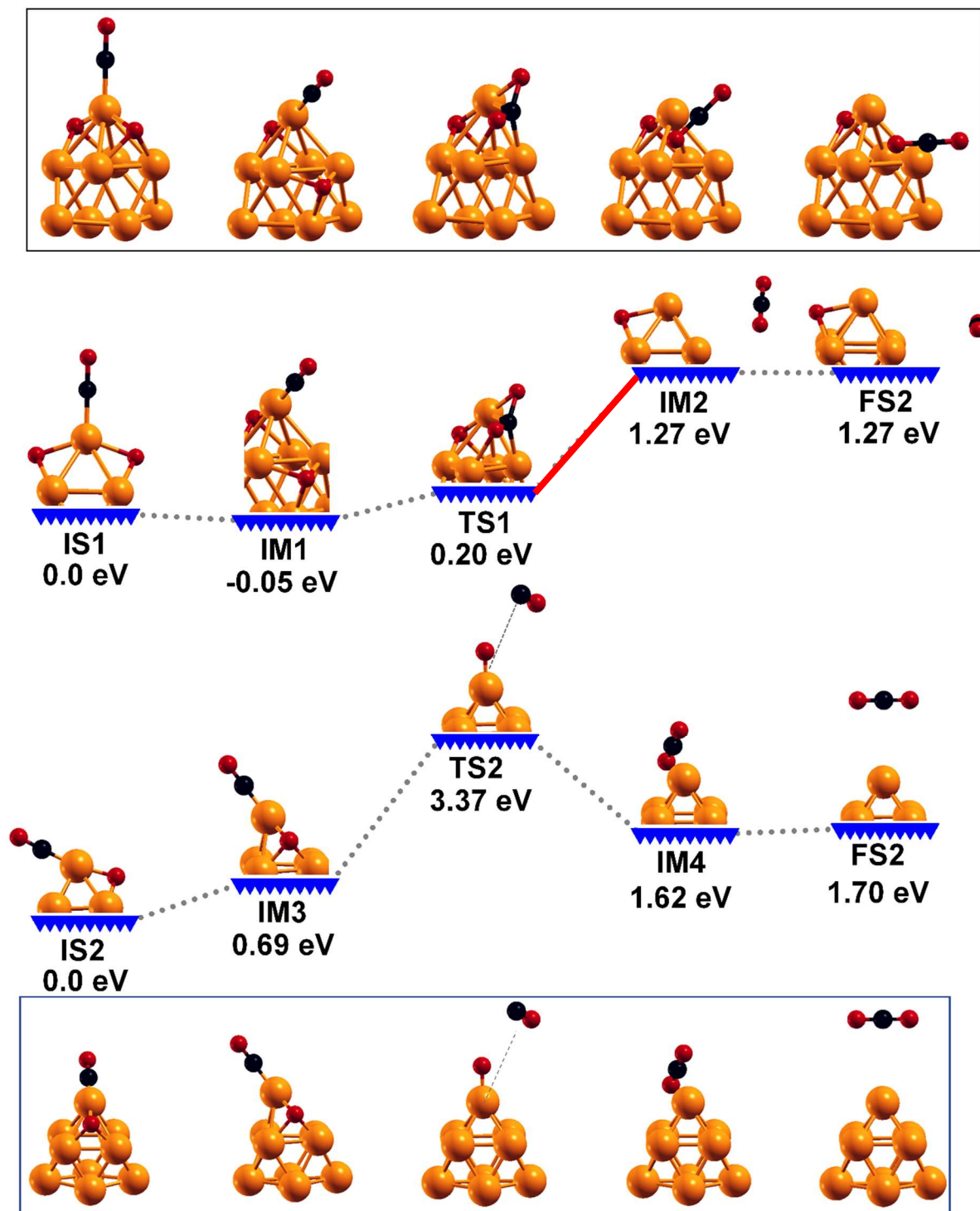
Figure 3.13: The complete L-H reaction pathway and activation barrier for CO oxidation over Ni$_9$ cluster. IS, IM, TS, and FS indicate initial state, intermediate state, transition state, and final state of reaction, respectively. The orange, black, and red balls represent Ni, C, and O atoms, respectively. The thermodynamically unfavored intermediates are connected with a red line.
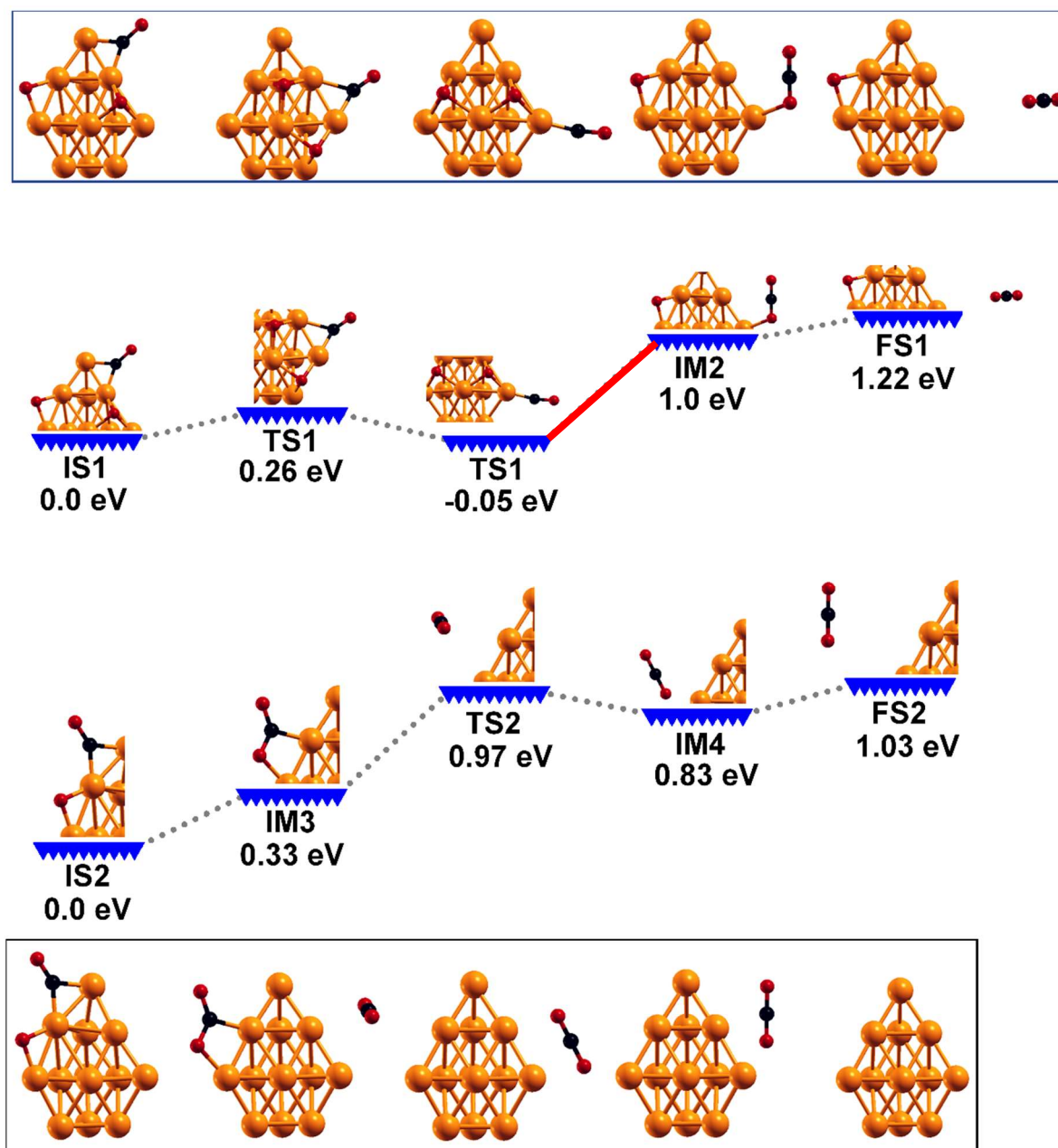
Figure 3.14: The complete L-H reaction pathway and activation barrier for CO oxidation over the Ni$_{13}$ cluster. IS, IM, TS, and FS indicate initial state, intermediate state, transition state, and final state of reaction, respectively. The orange, black, and red balls represent Ni, C, and O atoms, respectively. The thermodynamically unfavored intermediates are connected with a red line.
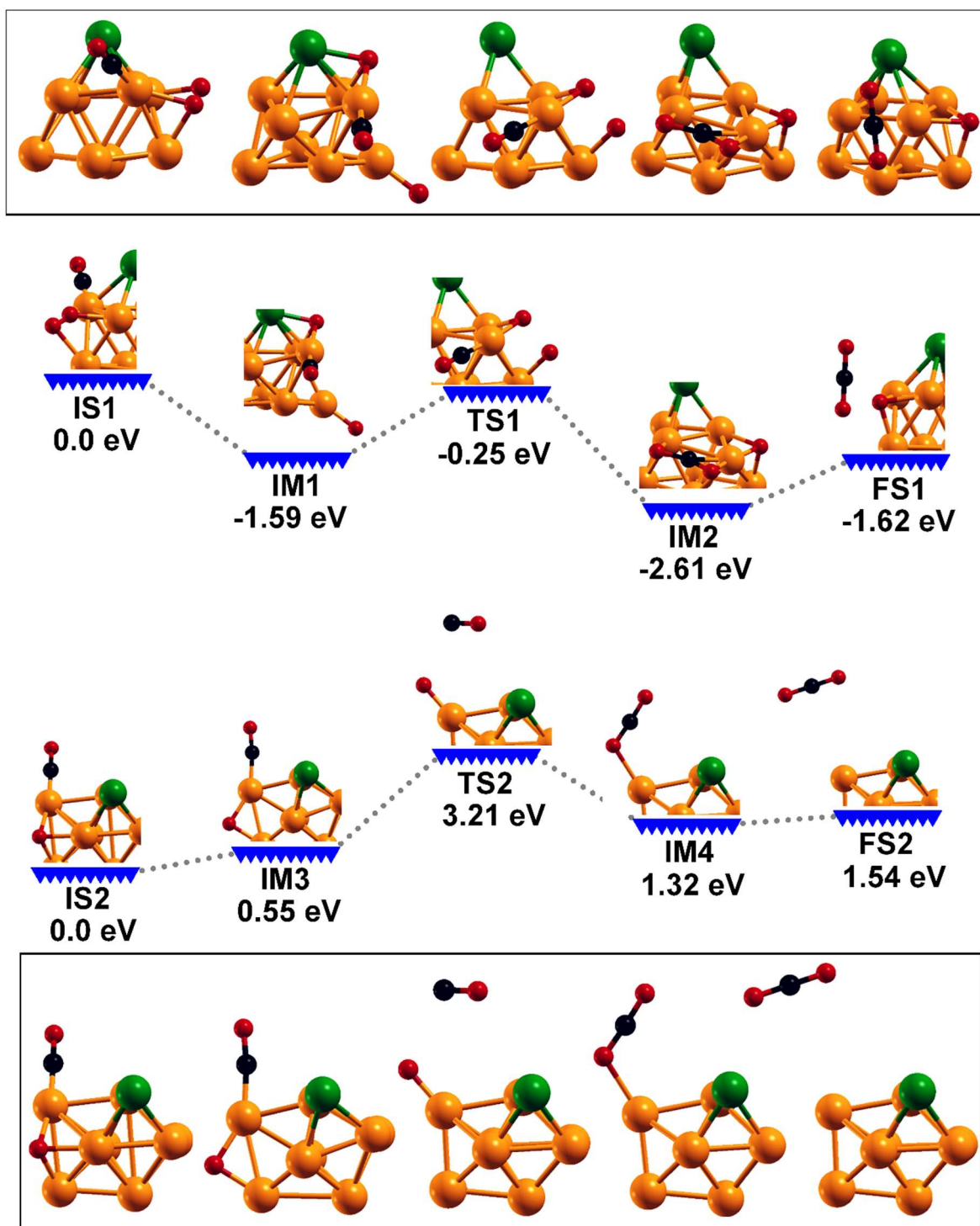
Figure 3.15: The complete L-H reaction pathway and activation barrier for CO oxidation over Ni_8Cu cluster. IS, IM, TS, and FS indicate initial state, intermediate state, transition state, and final state of reaction, respectively. The orange, green, black, and red balls represent Ni, Cu, C, and O atoms, respectively.
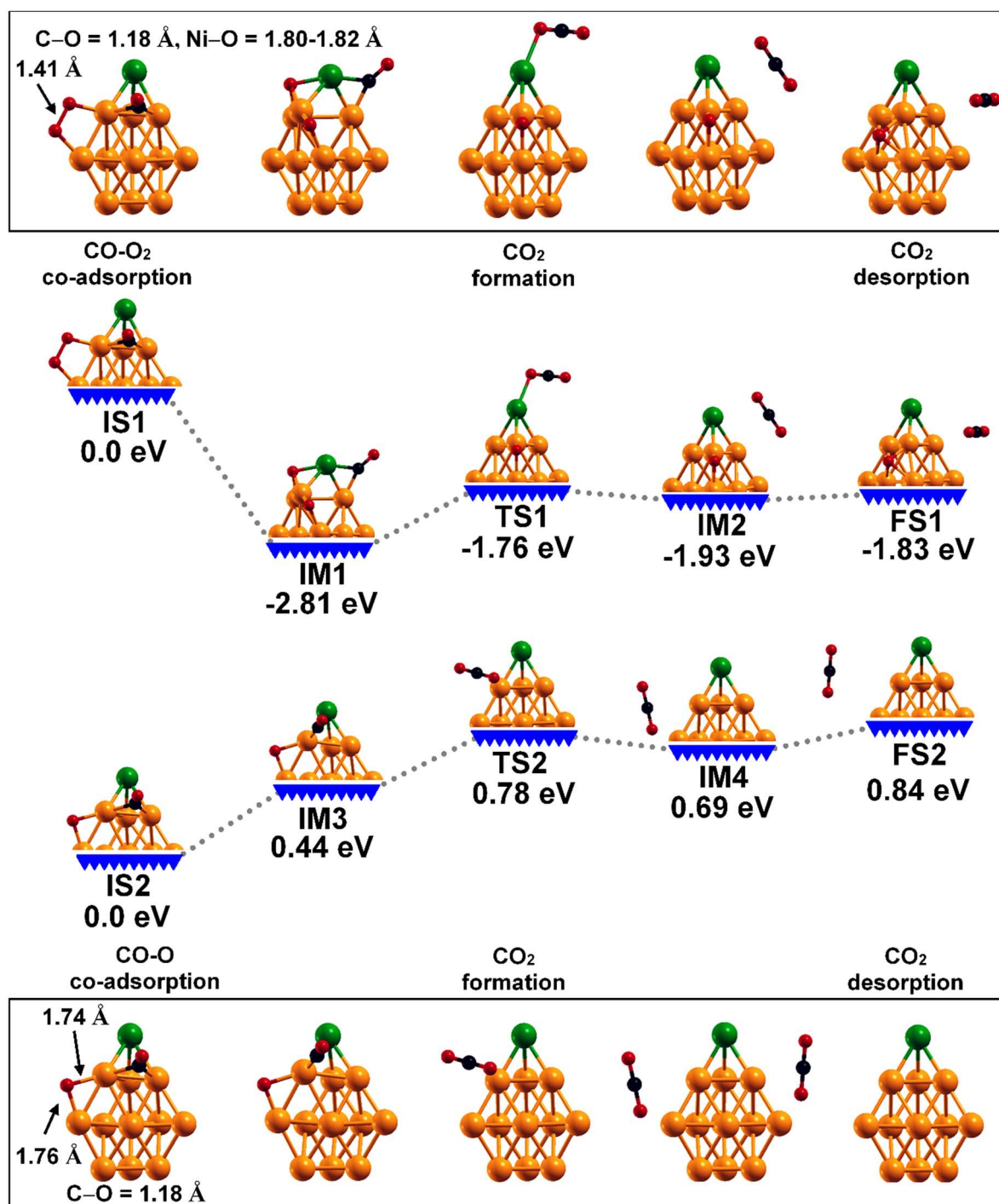
Figure 3.16: The complete L-H mechanism reaction pathway and activation barrier for CO oxidation onto the Ni$_{12}$Cu cluster. IS, IM, and TS indicate initial state, intermediate state, and final state of reaction respectively. The orange, green, black, and red atoms represent Ni, Cu, C, and O respectively.

Table 3.7: The co-adsorption energy (E_{ads}) of CO + O$_2$ (2O), CO + O, and activation energy barrier (E_a) for CO oxidation over Ni$_9$, Ni$_8$Cu, and Ni$_{13}$ clusters. The symbol * refers to the molecule/atom being adsorbed over the clusters.

System	co-adsorption	E_{ads} (eV)	
Ni$_9$	CO + O + O	-6.37	
	CO + O	-8.13	
Ni$_{13}$	CO + O + O	-6.81	
	CO + O	-1.09	
Ni$_8$Cu	CO + O$_2$	-4.53	
	CO + O	-7.64	
Ni$_{12}$Cu	CO + O$_2$	-4.67	
	CO + O	-1.00	
	Reaction		E_a (eV)
Ni$_9$	CO* + O*+ O* ↔ CO$_2$ + O*		0.20
	CO* + O* ↔ CO$_2$		3.37
Ni$_{13}$	CO* + O*+ O* ↔ CO$_2$ + O*		0.26
	CO* + O* ↔ CO$_2$		0.97
Ni$_8$Cu	CO* + O$_2$* ↔ CO$_2$ + O*		1.34
	CO* + O* ↔ CO$_2$		3.21
Ni$_{12}$Cu	CO* + O$_2$* ↔ CO$_2$ + O*		1.11
	CO* + O* ↔ CO$_2$		0.84

The complete reaction pathway of CO oxidation onto the Ni$_9$, Ni$_{13}$, Ni$_8$Cu, and Ni$_{12}$Cu clusters is depicted in Figures 3.13-3.16. Among the representative systems considered to perform CO oxidation, the flawless reaction profile is inspected for the Ni$_{12}$Cu cluster with the lowest activation barrier 1.11 eV (Ea_1) and 0.84 eV (Ea_2) for the first and second half-reactions, respectively. The value of co-adsorption energy of CO + O$_2$(2O), CO + O, and activation energy barrier (CO oxidation) for Ni$_9$, Ni$_{13}$, Ni$_8$Cu, and

Ni$_{12}$Cu clusters are presented in Table 3.7. Primarily, to facilitate the complete CO oxidation reaction, an oxygen molecule (O$_2$) was adsorbed on the CO-aided representative clusters (Ni$_9$, Ni$_{13}$, Ni$_8$Cu, and Ni$_{12}$Cu). Over Ni$_9$ and Ni$_{13}$ clusters, O$_2$ adsorbed dissociatively (2 × O) with -6.37 and -6.81 eV binding energies, respectively. O$_2$ prefers a side-on superoxo state (presented in Figure 3.15) to adsorb over Ni$_8$Cu and Ni$_{12}$Cu clusters with -4.53 and -4.67 eV binding energy, respectively. These representative clusters with co-adsorbed CO and O$_2$ (2O) onto them are then considered as an initial state (IS1) of reaction to perform CO oxidation and are shown in Figures 3.13-3.16.

In the first half-reaction (CO* + O$_2$* ↔ CO$_2$ + O*), the first transition state (TS1) displays the formation of CO$_2$ by breaking the O$_2$ superoxo bond with an activation barrier of 1.11 eV (exothermic process) and ejection of CO$_2$ molecule (FS1) is the end state of the first half-reaction. The asterisk indicates the adsorbed state of the adsorbate. For the second half-reaction (CO* + O* ↔ CO$_2$), the co-adsorption of CO + O (IS2) over representative systems was systematically performed for the initial state of the second-half reaction. After the first CO$_2$ molecule release, the remaining O is now activated on the Ni sites of the cluster which interacts with the new CO (TS2) and leads to the formation of another CO$_2$ with an activation barrier of 0.84 eV (endothermic process) to release the CO$_2$ from a cluster.

3.4 Conclusions

Following are the conclusions drawn from our spin-polarized DFT calculations.

(1)   The search initiated with the identification of the low-lying structure of Ni$_{n+1}$ and Ni$_n$Cu clusters using LDA and GGA functionals and our findings are consistent with earlier experimental and theoretical reports. We notice that the Cu atom prefers to stay at the low-connectivity vertex (or capped position) that minimizes the Ni−Cu bonds, which are weaker than Ni−Ni bonds. Therefore, the binding

energy per atom (E$_b$) slightly decreases after introducing the Cu atom to the clusters.

(2)   The low-intensity pre-edge peak (1s $\rightarrow$ 3d transition) positioned at around 8332−8335 eV in the XANES Ni K-edge spectra is consistent with the previously reported theoretical and experimental data. The decrement in the energy corresponding to both the rising-edge and the white line peaks confirmed the decrement in the oxidation state of Ni after introducing the Cu atom.

(3)   The calculation of mixing energy per atom (E_{mix}) displays the energetically preferred formation of Ni$_4$Cu, Ni$_6$Cu, Ni$_8$Cu, Ni$_{10}$Cu, and Ni$_{12}$Cu clusters among which the mixing of the Ni$_4$Cu cluster was found highly favorable with a maximum negative value of E_{mix}.

(4)   The calculated quantum chemical descriptors for Ni$_{n+1}$ and Ni$_n$Cu clusters are summarized in Appendix A.5.

(5)   For CO adsorption over Ni$_{n+1}$ and Ni$_n$Cu clusters, the PBE and PBE-D3 approaches were found capable of reproducing the experimentally preferred site as compared to other considered combinations. Except for a few cases, the magnitude of adsorption energy indicates the presence of the Cu atom which degraded the adsorption of CO molecule onto the Ni$_n$Cu clusters. This situation is mainly created by the charge transfer from the Cu to the Ni atom which makes Ni more efficient of charge and thus displays lower affinity toward the CO molecule. This is supposed to be responsible for degrading CO poisoning and improved catalytic activity.

(6)   The electronic reactivity descriptors for spin-up states ($\varepsilon_{d\uparrow}$) and spin-down states ($\varepsilon_{d\downarrow}$) of Ni were closer to the E$_F$ than that for the Cu atom. Thus, CO prefers Ni sites during adsorption on Ni$_n$Cu clusters.

(7)   The effective Löwdin charge analysis confirmed the occurrence of the donation−back-donation process in between the adsorbate-cluster systems.

(8)   The Ni$_{12}$Cu cluster stands out as a potential candidate for CO oxidation with the lowest activation barrier with negligible possibility of CO-poisoning over Ni.

The scope of our next work is to develop a strategy based on modifying an electronic structure (*d-band* center) for the poisoning-free mechanism of the TM alloys which will find its application in the fuel cells. Our results on the theoretical framework generate a novel strategy for the rational design of catalysts in essence to achieve poisoning-free CO oxidation over TM alloys.

References

1. H. J. Freund, G. Meijer, M. Scheffler, R. Schlögl, M. Wolf, *Angew. Chem. Int. Ed.* **50**, 10064-10094, (2011).

2. B. W. J. Chen, L. Xu, M. Mavrikakis, *Chem. Rev.* **121**, 1007-1048, (2021).

3. S. Dang, H. Yang, P. Gao, H. Wang, X. Li, W. Wei, Y. Sun, *Catal. Today* **330**, 61-75, (2009).

4. L. Liu, A. Corma, *Chem. Rev.* **118**, 4981-5079, (2018).

5. U. Heiz, A. Sanchez, S. Abbet, W. D. Schneider, *J. Am. Chem. Soc.* **121**, 3214-3217, (1999).

6. H. Hopster, H. Ibach, *Surf. Sci.* **77,** 109-117, (1978).

7. P. Trens, R. Durand, B. Coq, C. Coutanceau, S. Rousseau, C. Lamy, *Appl. Catal. B* **92***, 280-284, (2009).

8. J. J. Baschuk, X. Li, *Int. J. Energy Res.* **25**, 695-713, (2001).

9. M. T. Darby, E. C. H. Sykes, A. Michaelides, A. Stamatakis, *Top. Catal.* **61**, 428-438, (2018).

10. R. Ahmad, A. K. Singh, *ACS Catal.* **5**, 1826-1832, (2015).

11. W. Zhang, S. Shan, J. Luo, A. Fisher, J. F. Chen, C. J. Zhong, J. Zhu, D. Cheng, *J. Phys. Chem. C* **121**, 11010-11020 (2017).

12. X. L. Lei, M. S. Wu, G. Liu, B. Xu, C. Y. Ouyang, *J. Phys. Chem. A* **117**, 8293-8297, (2013).

13. J. R. Kitchin, J. K. Nørskov, M. A. Barteau, J. G. Chen, *J. Chem. Phys.* **120,** 10240-10246, (2004).

14. J. K. Nørskov, F. Abild-Pedersen, F. Studt, T. Bligaard, *Proc. Nat. Acad. Sci.* **108**, 937-943, (2011).

15. H. Xin, A. Vojvodic, J. Voss, J. K. Nørskov, F. Abild-Pedersen, *Phys. Rev. B* **89**, 115114-115119, (2014).

16. Y. Ishikawa, M. S. Liao, C. R. Cabrera, *Surf. Sci.* **513**, 98-110, (2002).

17. J. G. Wang, B. Hammer, *J. Catal.* **243**, 192-198, (2006).

18. V. P. Ananikov, *ACS Catal.* **5**, 1964-1971, (2015).

19. S. De, J. Zhang, R. Luque, N. Yan, *Energy Environ. Sci.* **9,** 3314-3347, (2016).

20. S. Dey, N. S. Mehta, *Chem. Eng. J. Adv.* **1**, 100008, (2020).

21. X. Hao, B. Wang, Q. Wang, R. Zhang, D. Li, *Phys. Chem. Chem. Phys.* **18**, 17606-17618, (2016).

22. R. V. de Amorim, K. E. A. Batista, G. R. Nagurniak, R. P Orenha, R. L. T. Parreira, M. J. Piotrowski, *Dalton Trans.* **49**, 6407-6417 (2020).

23. J. C. M. Harberts, A. F. Bourgonje, J. J. Stephan, V. Ponec, *J. Catal.* **47**, 92-99, (1977).

24. K. M. Gameel, I. M. Sharafeldin, N. K. Allam, *Phys. Chem. Chem. Phys.* **21**, 11476-11487, (2019).

25. P. Giannozzi, S. Baroni, N. Bonini, M. Calandra, R. Car, C. Cavazzoni, D. Ceresoli, G. L. Chiarotti, M. Cococcioni, I. Dabo, et al., *J. Phys.: Condens. Matter* **21**, 395502-395521, (2009).

26. P. Giannozzi, O. Andreussi, T. Brumme, O. Bunau, M. Buongiorno, M. Nardelli, M. Calandra, R. Car, C. Cavazzoni, D. Ceresoli, M, Cococcioni, et al., *J. Phys.: Condens. Matter* **29**, 465901-465930, (2017).

27. G. Kresse, D. Joubert, *Phys. Rev. B* **59**, 1758-1775, (1999).

28. J. P. Perdew, A. Zunger, *Phys. Rev. B* **23**, 5048-5079, (1981).

29. J. P. Perdew, K. Burke, M. Ernzerhof, *Phys. Rev. Lett.* **77**, 3865-3868, (1996).

30. M. Methfessel, A. T. Paxton, *Phys. Rev. B* **40**, 3616-3621, (1989).

31. J. D. Head, M. C. Zerner, *Chem. Phys. Lett.* **122**, 264-270, (1985).

32. J. P. Chou, C. R. Hsing, C. M. Wei, C. Cheng, C. M. Chang, *J. Phys.: Condens. Matter* **25**, 125305-125312, (2013).

33. R. Hoppe, *Angew. Chem. Int. Ed.* **9**, 25-34, (1970).

34. S. Grimme, *J. Comput. Chem.* **27**, 1787-1799, (2006).

35. S. Grimme, J. Antony, S. Ehrlich, H. A. Krieg, *J. Chem. Phys.* **132**, 154104-154119, (2010).

36. S. Baroni, S. de Gironcoli, A. D. Corso, P. Giannozzi, *Rev. Mod. Phys.* **73**, 515-562, (2001).

37. B. Hammer, J. K. Nørskov, *Adv. Catal.* **45**, 71-129, (2000).

38. S. Bhattacharjee, U. V. Waghmare, S. C. Lee, *Sci. Rep.* **6**, 35916-35926, (2016).

39. G. Henkelman, H. Jónsson, *J. Chem. Phys.* **113**, 9978-9985, (2000).

40. G, Henkelman, B. P. Uberuaga, H. A. Jónsson, *J. Chem. Phys.* **113**, 9901-9904, (2000).

41. A. Kokalj, *J. Mol. Graphics Modell.* **17**, 176-179, (1999).

42. K. Momma, F. Izumi, *J. Appl. Crystallogr.* **44**, 1272-1276, (2011).

43. M. D. Morse, *Chem. Rev.* **86**, 1049-1109, (1986).

44. E. M. Spain, M. D. Morse, *J. Chem. Phys.* **97**, 4633-4640, (1992).

45. M. Castro, C. Jamorski, D. R Salahub, *Chem. Phys. Lett.* **271**, 133-142, (1997).

46. A. Granja-DelRio, H. A. Abdulhussein, R. L. Johnston, *J. Phys. Chem. C* **123**, 26583-26596, (2019).

47. M. Boulbazine, A. G. Boudjahem, M. Bettahar, *Mol. Phys.* **115**, 2495-2507, (2017).

48. P. L. Rodríguez-Kessler, A. R. Rodríguez-Domínguez, *J. Phys. Chem. C* **119**, 12378-12384 (2015).

49. P. A. Derosa, J. M. Seminario, P. B. Balbuena, *J. Phys. Chem. A* **105**, 7917-7925, (2001).

50. Y. Joly, *Phys. Rev. B* **63**, 125120-125130, (2001).

51. O. Bunau, Y. Joly, *J. Phys.: Condens. Matter* **21**, 345501-345512, (2009).

52. A. Anspoks, A. Kuzmin, *J. Non-Cryst. Solids* **357**, 2604-2610, (2011).

53. B. Zandkarimi, G. Sun, A. Halder, S. Seifert, S. Vajda, P. Sautet, A. N. Alexandrova, *J. Phys. Chem. C* **124**, 10057-10066, (2020).

54. K. E. A. Batista, J. L. F. Da Silva, M. J. Piotrowski, *J. Phys. Chem. C* **123**, 7431-7439, (2019).

55. B. A. Baraiya, V. Mankad, P. K. Jha, *Spectrochim. Acta A* **229**, 117912-117920, (2020).

56. L. Grajciar, P. Nachtigall, O. Bludský, M. Rubeš, *J. Chem. Theory Comput.* **11**, 230-238, (2015).

57. K. P. Huber, G. Herzberg, Molecular Spectra and Molecular Structure Constants of Diatomic Molecules, Springer US, (1979).

58. K. Bleakley, P. A. Hu, *J. Am. Chem. Soc.* **121**, 7644-7652, (1999).

59. P. S. Bagus, C. J. Nelin, C. W. Bauschlicher, *Phys. Rev. B*, **28**, 5423, (1983).

60. Z. H. Zeng, J. L. F. Da Silva, W. X. Li, *Phys. Chem. Chem. Phys.* **12**, 2459-2470, (2010).

61. A. S. Chaves, M. J. Piotrowski, D. Guedes-Sobrinho, J. L. F. Da Silva, *J. Phys. Chem. A* **119**, 11565-11573, (2015).

62. S. Rai, M. Ehara, U. D. Priyakumar, *Phys. Chem. Chem. Phys.* **17**, 24275-24281, (2015).